Supplementary Materials for

Transforming a CO_2 Adsorbent to a Superior and Robust RWGS Catalyst by Controlling MgO Defects with Ce Single Atoms

Shiyan Li [1,2,†], Na Li[3,†], Tian Qin[4,†,] Zhanglong Guo[1], Yuan Lv[1], Riguang Zhang[3,]*, Xi Liu[4,*],
Liwei Chen,[4] Siglinda Perathoner[5], Gabriele Centi[5,*], Yuefeng Liu[1,*]

[1] Dalian National Laboratory for Clean Energy (DNL), Dalian Institute of Chemical Physics, Chinese Academy of Science,457 Zhongshan Road, Dalian 116023, China
[2] University of Chinese Academy of Sciences, Beijing 100049, China
[3] State Key Laboratory of Clean and Efficient Coal Utilization, College of Chemical Engineering and Technology, Taiyuan University of Technology, Taiyuan, China
[4] School of Chemistry and Chemical, In-situ Center for Physical Science, Shanghai Jiao Tong University, Shanghai, China
[5] Department ChiBioFarAm, University of Messina, v.le F. Stagno D'Alcontres 31, 98166 Messina, Italy

**Corresponding author.*
Riguang Zhang, email: zhangriguang@tyut.edu.cn
Xi Liu, email: liuxi@sjtu.edu.cn
Gabriele Centi, email: centi@unime.it
Yuefeng Liu, email: yuefeng.liu@dicp.ac.cn

The PDF file includes:

Materials and Methods

Preparation of Ce-MgO-D(x) catalysts

A series of Ce-MgO catalysts with different Ce dosages were prepared using the citrate complex method. Taking the synthesis procedure of Ce-MgO-D(1.6) catalyst as an example: 0.12 mmol cerium nitrate hexahydrate, 24.5 mmol magnesium nitrate hexahydrate precursors and 49.3 mmol citric acid were dissolved in 20 mL deionised water and stirred at room temperature for 4 h. The mixed solution of precursors was then transferred to a rotary evaporator for rotary evaporation. After 2 h evaporation, the resultant sol was dried overnight in an oven at 120^{o}C. The obtained powders were ground and calcined in the Muffle furnace at 650 °C for 2 h with a ramping rate of 5^{o}C·min^{-1}. All of the as-prepared catalysts were denoted as Ce-MgO-D(x), where x represents the weight fraction of Ce. The molar ratio of citric acid to metals (Mg and Ce) was fixed at 2. In addition, pure MgO and pure CeO_2 were also prepared according to the procedures mentioned above.

Preparation of reference catalysts

CeNPs-MgO-D: The catalyst was prepared using the impregnation method, including the preparation of CeO_2 NPs. CeO_2 NPs were synthesised from the decomposition of cerium nitrate hexahydrate at high temperatures, which is referred to in the previous reports.[1,2] Briefly, 5 mmol of cerium nitrate hexahydrate and 15 mmol of oleylamine as a stabilising agent were mixed in 30 mmol 1-octadecene at room temperature. After vigorous stirring at 80^{o}C for 1 h under a nitrogen (N_2) gas environment, the temperature was ramped to 200^{o}C and maintained for 2 h. The obtained colloid was washed using ethanol, acetone and hexane 5 times after cooling and dispersed in 100 mL of hexamethylene.

The CeNPs-MgO-D catalyst was prepared using the impregnation (IMP) method. 1 g MgO-D support and 9.14 mL CeO_2 NPs solution were dispersed in 30 mL hexamethylene and stirred at room temperature for 1 h. The suspension was then transferred to a rotary evaporator for rotary evaporation and dried at 110^{o}C overnight. The solid was calcined at 350 °C for 3 h to obtain the final catalyst.

Ce-SiO_2: The catalyst was prepared using the impregnation (IMP) method. 1 g SiO_2 support and 0.12 mmol cerium nitrate hexahydrate were added to 30 mL deionised water and stirred at room temperature for 3 h. After removing the solvent, the obtained powders were treated at 110^{o}C overnight. Then, the solid was calcined at 650^{o}C for 2 h in the Muffle furnace to obtain the final catalyst.

Ce-Al_2O_3: The catalyst was prepared using the citrate complex method. 0.12 mmol cerium nitrate hexahydrate, 9.6 mmol aluminium nitrate hexahydrate precursors and 29.2 mmol citric acid were dissolved in 20 mL deionised water and stirred at room temperature for 4 h. The mixed solution of precursors was then transferred to a rotary evaporator for rotary evaporation. After 2 h evaporation, the resultant sol was dried overnight in an oven at 120^{o}C. The obtained powders were ground and calcined in the Muffle furnace at 650°C for 2 h with a ramping of 5^{o}C/min.

CuZnAl: The catalyst was prepared using the urea homogeneous precipitation method.[3] Typically, 12.50 mmol copper nitrate trihydrate, 3.12 mmol zinc nitrate hexahydrate, 2.08 mmol aluminium nitrate hexahydrate, and 200 mmol urea were dissolved in 100 mL deionised water and stirred at 95 °C for 2 h. The obtained slurry was aged at 95°C for 24 h and then filtered and washed with deionised water three times. Finally, the CuZnAl catalyst was obtained after drying in an oven at 60°C for 12 h and then calcination in static air at 350°C for 3h.

Characterisation

Powder X-ray Diffraction (PXRD). The PXRD results were collected on an X'pert-Pro diffractometer (PAN Analytical, Netherlands) using Cu Kα radiation ($\lambda = 1.54$ Å) at 40 kV and 40 mA in the range of 10 - 90°.

Inductively Couple Plasma-Optical Emission Spectroscopy (ICP-OES). Elemental contents were measured with ICP-OES using a PerkinElmer 7300DV analyser.

Transmission Electron Microscopy (TEM). TEM measurements were carried out on a JEM-2100 operating at an accelerated voltage of 200 kV.

Scanning Transmission Electron Microscopy (STEM). The atomic resolution STEM with ADF detection and field emission scanning electron microscopy (FESEM) were performed on an HF5000 microscope from the Hitachi Company with a 200 kV cold-field emission gun and a Cs-corrector for the electron probe. The EELS spectra were acquired with a Gatan GIF camera. An energy dispersion of 0.25 eV was used to acquire the Ce L-edge, with an energy resolution of approximately 1 eV. For core-loss acquisition, the pixel size was set to 2 Å × 2 Å and the dwell time to 0.5 s. The EELS spectrum of CeO_2 particles was used as a reference. As complementary to the STEM microscopy, the STEM images and element mapping images were collected by JEM ARM200F thermal-field emission microscope with a probe spherical aberration (Cs) corrector working at 200kV. The samples were ultrasonicated in an ethanol solution, dropped onto the copper grid covered with a holey carbon membrane and dried for observation.

EELS analysis

Due to the extremely weak signal of Ce single atoms, we manually selected individual spectra with a significant Ce signal and summed them to enhance the SNR.

The valence state of Ce was determined by calculating the M5/M4 ratio. First, a power-law model was fitted to remove the background of the raw spectra. Then, a double arctan function was used to remove the continuum background in the EELS spectra. The areas of M5 and M4 were integrated within an 8 eV-wide window, and the M5/M4 ratio was calculated. The M5/M4 ratio of the Ce single atom was compared with that of the CeO_2 (IV) reference to determine the valence state.

Electron Paramagnetic Resonance (EPR). The EPR spectra were gained from Bruker A200 spectrometer at room temperature.

Ultraviolet-Visible Spectroscopy (UV-vis). The catalysts' UV-vis absorption spectra were measured at room temperature using a Perkin Elmer Lambda950 UV-vis near-infrared spectrometer (200 - 800 nm at a 10 nm/s scan rate).

Temperature-Programmed Desorption of CO_2 (CO_2-TPD). The CO_2-TPD experiments were performed on a fixed bed reactor with a U-shaped quartz tube (inner diameter 6 mm) at atmospheric pressure, with the signals recorded by a QMD mass spectroscopy. First, a 100 mg catalyst was pretreated at 500°C for 1 h under the flow of 99.99% He (40 $mL\cdot min^{-1}$) and then cooled down to 50°C. After that, the 100 vol% CO_2 (40 $mL\cdot min^{-1}$) was passed through the catalyst for 1 h during adsorption, followed by flushing in He for 1 h with 30 $mL\cdot min^{-1}$ to remove the physically adsorbed CO_2. Finally, the catalyst was heated to 600 °C at 10°C·min^{-1} under He flow at 30 mL·min^{-1}, and the desorbed CO_2 was monitored with mass spectroscopy.

Temperature-Programmed Surface Reaction (TPSR). The TPSR characterisation of CO_2/H_2 was carried out on a fixed-bed reactor, and then the reactor was inspected online using a QMD mass spectrometer. 100 mg of catalyst was loaded in a U-shaped quartz tube (inner diameter 6 mm) reactor. It was pretreated in H_2 for 1 h and in He for 1 h at 500 °C, respectively. After cooling down to 50 °C in He, the reactants with a molar ratio of $CO_2/H_2/N_2$ = 5/15/80 were introduced at a flow rate of 40 mL·min^{-1}. The temperature of the reactor was started from 50 °C to 800 °C with a ramp of 10 °C·min^{-1}.

H_2-D_2 exchange Reaction. H_2-D_2 exchange reactions were performed on a temperature-programmed micro-fixed bed reactor equipped with a mass spectrometer. Typically, 100 mg of the sample was reduced in H_2 (30 mL·min^{-1}) at 500 °C for 1 h, then the gas was switched to Ar (30 mL·min^{-1}) and treated at 500 °C for 1 h, followed by cooled down in Ar until the baseline signal in MS spectra was steady at 30 °C. At that time, a mixture of D_2 (5 mL·min^{-1}), H_2 (5 mL·min^{-1}) and Ar (20 mL·min^{-1}) was introduced into the catalyst sample and kept for ~30 min at 30 °C. Next, the catalyst was heated to 300 °C with a heating rate of 10°C·min^{-1}. A mass detector (QMD) was used to analyse the signal of m/z = 2 (H_2), 3 (HD) and 4 (D_2).

Nearly-*in-situ* X-ray photoelectron spectroscopy (XPS). Nearly-in-situ XPS analyses were performed on a Thermofisher Escalab 250 Xi+ photoelectron spectroscope equipped with a monochromatic Al Kα radiation. All the binding energies were calibrated to the containment carbon C 1s peak (284.8 eV). The data analysis was performed using CasaXPS and a Shirley background.

X-ray Absorption Spectroscopy (XAS). The XAS experiments, including X-ray absorption near edge spectra (XANES) and extended X-ray absorption fine structure (EXAFS) of Ce L_3-edge, were collected at the BL11B beamline of the Shanghai Synchrotron Radiation Facility (SSRF). Before the measurement, the samples were pressed into the table. The data from the prepared catalysts and references were collected at room temperature under transmission mode. The acquired XAS data were processed according to standard procedures using the ARTEMIS module implemented in the IFEFFIT software package.

***In-situ* Diffuse Reflectance Infrared Fourier Transforms (DRIFTS) spectroscopy**. The *In-situ* DRIFTS investigations were recorded using a Bruker Vertex 80V spectrometer equipped with a Mercury-Cadmium-Tellurium (MCT) detector in the range 850-4000 cm^{-1} at a 32-scan integral at a resolution of 4 cm^{-1}. For CO_2 adsorption, the catalyst was pretreated with H_2 at 500 °C for 2 h sequentially in Ar for 1 h. The background spectrum was obtained at 500, 400, 300 and 200°C and then at r.t. (30°C) in Ar flow. After cooling the catalyst down to room temperature (RT), the gas flow was changed to 5% CO_2/Ar (40 mL·min^{-1}, 0.1 MPa), and the spectra were collected simultaneously. Once the adsorption was completed (that is, the intensity of CO_2-adsorption bands no longer increased), the temperature was increased from 30 °C to 500 °C in 5% CO_2/Ar (40 mL·min^{-1}, 0.1 MPa), and the spectrum was continuously recorded. The reaction DRIFTS spectra and H-D isotope exchange DRIFT spectra were obtained using a similar procedure. The catalyst was pretreated with H_2 at 500 °C for 2 h sequentially in Ar for 1 h. The reaction infrared spectra were continuously recorded during exposure to 5 vol% CO_2/15 vol% H_2/80 vol% Ar. The H-D isotope exchange DRIFT spectra were continuously recorded during exposure to D_2.

DFT calculations.

Computational methods: All spin-polarised DFT calculations were carried out using the Vienna Ab-initio Simulation Package (VASP) [4,5]. The Perdew-Burke-Ernzerhof (PBE) functional within the Generalised Gradient Approximation (GGA)[6] was used to describe the exchange and correlation effects. Valence electrons were described using plane waves with a kinetic energy cutoff of 400 eV, while core electrons were treated with the Projector Augmented Wave (PAW) method.[7] The dispersion-corrected DFT-D3 method was employed to describe the van der Waals (vdW) interactions.[8] U_{eff} = 5.0 eV was applied to the Ce 4f states to calculate the highly localised Ce 4f orbitals accurately.[9] The Brillouin zone was sampled using 8 × 8 × 1 and 3 × 3 × 1 Monkhorst-Pack *k*-points mesh for the bulk of MgO and surface models, respectively. The convergence criteria for the forces and total energy were set at 0.02 eV/Å and 1.0×10^{-5} eV, respectively. The Climbing Image Nudged Elastic Band (CI-NEB) method[10,11] was employed to search the transition states (TSs), and then, the dimer method[12,13] was used to locate the transition state until the energy converged to 0.03 eV/Å. All transition states were verified by vibrational frequency analysis. All energies of the elementary step involved in the RWGS reaction are corrected at 873.15 K.

Computational models: The optimised lattice parameters (a = b = c = 4.20 Å) of MgO bulk were in excellent agreement with the experimental values (a = b = c = 4.21 Å).[14] The MgO(100) surface was modelled using a *p*(3 × 3) supercell consisting of four atomic layers named as MgO. The defective MgO(100) surface (denoted as MgO-D) was constructed by removing some atoms from the MgO surface to induce a step structure. The Ce atom-doped defective MgO(100) surface (denoted as Ce-MgO-D) was constructed by substituting an Mg atom at the step sites of the MgO-D surface with a Ce atom. The defective MgO(100) surface with enriched oxygen-vacancy (denoted as O_v-MgO-D) and Ce atom-doped defective MgO(100) surface with enriched oxygen-vacancy (denoted as Ce-O_v-MgO-D) were further constructed by removing an oxygen atom from the step sites of MgO-D surface to simulate the observed oxygen vacancies. A similar approach has been successfully applied in previous studies about the surface and catalytic properties of MgO.[15,16] In all calculations, all atoms were relaxed except for the bottom two atomic layers. For all surface models, a vacuum layer of 15 Å was added in the vertical direction to avoid interlayer interactions. Detailed structures of these surface models are shown later in Figure S25.

Catalytic performance evaluation and kinetic experiments.

The CO_2 hydrogenation reaction was carried out at ambient pressure in a quartz tube reactor (d = 8 mm) under a gas atmosphere of 24% CO_2/72% H_2/N_2 (40 $mL\cdot min^{-1}$) with the GHSV of 24,000 $mL\cdot g_{cat.}^{-1}\cdot h^{-1}$. Before the activity test, 100 mg catalysts (160 - 400 µm) with 1.0 g SiC (400 - 450 µm) as a diluent were activated by 100% H_2 (40 $mL\cdot min^{-1}$) at 500 °C for 2 h at a ramp of 5 $^{o}C\cdot min^{-1}$. After the reduction, the H_2 stream was switched to Ar until the temperature was heated to 600 °C, and the reactant gas was switched to pass through the catalyst bed. The effluent gas was analysed online by an Agilent 7890B gas chromatography (GC) instrument equipped with a thermal conductivity detector (TCD). The long-term stability of the catalyst was also measured at 600^{o}C for 150 h duration. CO_2 conversion, CO selectivity and RWGS rate were calculated by using the following equations:

$$\mathrm{Conversion}\ (\mathrm{CO_2},\%) = \left(1 - \frac{\mathrm{F_{CO_2,out}}}{\mathrm{F_{CO_2,in}}}\right) \times 100\% \qquad (1)$$

$$\text{Selectivity (CO, \%)} = \frac{F_{CO,out}}{F_{CO_2,in} - F_{CO_2,out}} \times 100\% \tag{2}$$

$$\text{RWGS rate } (\text{umol} \cdot g_{cat.}^{-1} \cdot s^{-1}) = \frac{F_{CO_2,in} - F_{CO_2,out}}{m_{cat.}} \tag{3}$$

where $F_{CO_2,in}$ is the concentration of CO_2 in the reaction stream, and $F_{CO_2,out}$, $F_{CO,out}$ are the concentrations of CO_2 or CO (respectively) in the outlet stream. $m_{cat.}$ (g) represents the mass of the catalyst during the catalytic performance test.

The kinetic experiments were performed in the same reactor. The CO_2 conversion was kept below 15% by adjusting gas hourly space velocity (GHSV) to eliminate any diffusion resistance. The reaction order with respect to reactants (CO_2 and H_2) was obtained at 500^{o}C, and changing the flow rate of H_2 between 6-72 mL·min^{-1}, the flow rate of CO_2 between 6-72 mL·min^{-1}, while using N_2 as a balance to maintain a 100 mL·min^{-1} total flow rate. The apparent activation energy was measured similarly.

Supplementary Text

Theoretical modelling of H_2 adsorption and dissociation.

H_2 adsorption and dissociation over MgO, MgO-D, Ce-MgO-D, O_v-MgO-D, and Ce-O_v-MgO-D were investigated theoretically. The corresponding optimised configurations and potential energy profiles for H_2 adsorption and dissociation are shown in Figures S28-S30. Specifically, H_2 molecules are physically adsorbed on the MgO, MgO-D, and Ce-MgO-D catalysts. Then, the dissociation of physically adsorbed H_2 was further analyzed (Figure S30a). The two H atoms from H_2 heterolytic dissociation were adsorbed at the Mg site and O site, respectively, and the dissociation activity followed the order of MgO (2.50 eV) < Ce-MgO-D (0.80 eV) < MgO-D (0.43 eV). Interestingly, the presence of oxygen-vacancies over O_v-MgO-D and Ce-O_v-MgO-D catalysts promotes spontaneous dissociation of H_2 molecules, and it is strongly exothermic; correspondingly, the co-adsorption energy of two H atoms is more negative (Figure S30b). The above results indicate that compared to the five-coordinated oxygen sites (O_{5C}) in the MgO catalysts, the presence of four-coordinated oxygen atoms on the surfaces of MgO-D and Ce-MgO-D can lower the activation barriers for H_2 dissociation. In contrast, the presence of oxygen vacancy on the O_v-MgO-D and Ce-O_v-MgO-D surface further enhanced the H_2 dissociation activity, suggesting that the presence of unsaturated-coordinated oxygen sites (O_{4C}) and oxygen vacancy are the key factors for the enhancement of H_2 dissociation ability.

H_2-D_2 exchange reactions were studied over the MgO-C, MgO-D and Ce-MgO-D(1.6) catalysts. After activation in the H_2 atmosphere at 500^{o}C, a mixture of H_2 and D_2 (5 mL·min^{-1} and 5 mL·min^{-1}, respectively) was introduced into the catalyst bed. For the Ce-MgO-D(1.6) catalyst (Figure S31), the formation of HD (e.g. hydrogen molecule with one hydrogen and one deuterium atom) occurred at 50^{o}C, which has a higher HD signal than MgO-C and MgO-D catalysts, indicating that the activation of the H-H bond in H_2 on Ce doped MgO was much more facile than pure MgO.

XRD and HRTEM results

The XRD (Figure S1) and HRTEM (Figure S13) results of MgO revealed that the (100) plane was the main exposed surface. This surface was used in the following calculation and simulation, which were not changed after the addition of Ce species (Figure S13b).

Catalytic behavior

The catalytic performances in the RWGS reaction over Ce-MgO-D(1.6) and MgO-C catalysts were evaluated at various temperatures with a space velocity of 24,000 mL·$g_{cat.}^{-1}$·h^{-1} under the conditions of 24% CO_2, 72% H_2 and N_2 as equilibrium gas. First, we tested the catalytic performance of quartz with a CO_2 conversion of 0.9% at 600°C. The commercial MgO (MgO-C, Macklin) show a negligible RWGS catalytic performance, where the CO_2 conversion is as low as 6.5% at 600°C (Figure S16). The activity of MgO-C was reduced to 3.4% (Figure S16) after treatment at 1200°C, indicating that sintering may occur after high-temperature treatment of MgO-C, resulting in a decrease in the number of active sites. Besides, the Ce-MgO-D(1.6) catalyst showed a very promising performance, which can reach equilibrium conversion at higher reaction temperature with a space velocity of 4800 mL·$g^{-1}_{cat.}$·h^{-1} (Figure S16).

Combining RWGS and Fischer-Tropsch synthesis is considered the most promising process for converting CO_2 to value-added chemicals.[17] Thus, we performed Ce-MgO-D(1.6) catalyst at a high pressure of 10 and 20 bar (Figure S18). The CO_2 reduction performance of defective MgO-D nanoparticles is 5.5-8.3 times higher than that of MgO-C. When the Ce species is introduced, the CO_2 activity gradually increases to 18.9 μmol·$g_{cat.}^{-1}$·s^{-1} at 20 bar. Interestingly, the MgO-D and Ce-MgO-D(1.6) catalysts have >98.5% CO selectivity in the pressure range of 1- 20 bar, whereas the MgO-C catalysts have only 85.4% CO selectivity at 20 bar.

Kinetic results

In order to further explore the catalytic process, the Arrhenius plots of MgO-D and Ce-MgO-D(1.6) catalysts were obtained (Figure S19). The apparent activation energy (Ea) of the three catalysts indicates a value of about 105-110 kJ mol^{-1} for MgO-C, MgO-D and Ce-MgO-D(1.6) (Figure S19a and Table S4). Subsequently, the apparent reaction orders of the CO_2 and H_2 were investigated by varying the partial pressure of the reactants at 500°C. As shown in Figure S19b and Table S4, the reaction orders of CO_2 and H_2 were estimated to be -0.78 and 0.57, respectively. The reaction rates of CO_2 increased with the partial pressure of H_2, while the reaction rates of CO_2 were suppressed in excess of CO_2.

The apparent activation energy (Ea) for the three catalysts was the same value (Figure S19a), but Ce-MgO-D(1.6) exhibits a higher CO_2 reaction rate (37.2 μmol·$g_{cat.}^{-1}$·s^{-1}) than that of MgO-C (4.6 μmol·$g_{cat.}^{-1}$·s^{-1}) and MgO-D (26.4 μmol·$g_{cat.}^{-1}$·s^{-1}). Therefore, we continued to correlate the CO_2 reaction rate with the fraction of oxygen defects and rate constant k_{app} in Figure S20. It was found that the CO_2 reaction rate had good linearity on the fraction of oxygen defects (Figure S20a) and rate constant k_{app} (Figure S20b), indicating the difference is related to the pre-exponential factors (the number of active sites, Table S4).[18]

Characterisation of the catalysts after the stability tests

Powder x-ray diffraction (PXRD) analysis of the catalyst recovered after the long-term stability test revealed no discernable diffraction peaks of CeO_2 crystals (Figure S39), indicating that the Ce species were highly dispersed on MgO for cerium loadings as high as 4 wt% after reaction.

Comparisons between TEM and STEM-HAADF images of the fresh and spent catalysts do not reveal apparent changes in the material and single-dispersed Ce species upon prolonged exposure to reactants under these harsh conditions (Figures S40 and S41). In addition, STEM-HAADF images collected before and after the reaction illustrated the Ce species disperse in a single-atom form on the MgO (100) surface, illustrating that the structure of the Ce-MgO-D catalysts is very stable during the reaction.

These observations suggest that its prolonged high activity may result from the lack of aggregation or structural transformation during long exposure to the reaction conditions.

Supplementary Results

Additional characterisation data

Table S1. Elementary Content of Ce in Ce-MgO-D Catalysts Characterized by ICP-OES. TA: theoretical amount.

Catalysts	**$Ce_{(TA)}$/wt%**	**$Ce_{(ICP)}$/wt%**
MgO-D	0	-
Ce-MgO-D(0.2)	0.16	0.12
Ce-MgO-D(0.4)	0.41	0.33
Ce-MgO-D(0.8)	0.81	0.75
Ce-MgO-D(1.6)	1.63	1.44
Ce-MgO-D(4)	4.07	3.10
CeO_2	100	-

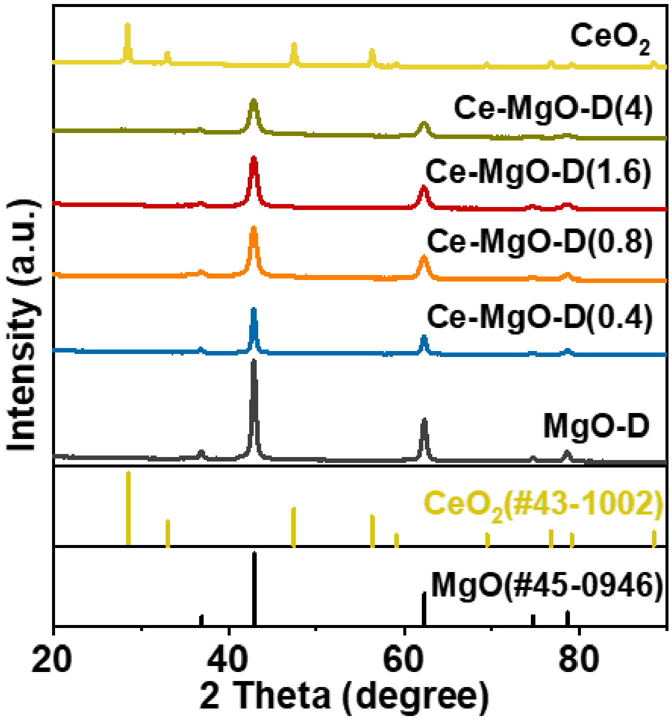

Figure S1. XRD patterns of Ce-MgO-D samples with different cerium content. Diffraction peaks of face-centred cubic MgO (JCPDS No. 45-0946) dominate in all Ce-MgO-D samples with different cerium content. No discernable diffraction peaks for CeO_2 crystals were observed, indicating that the Ce species were highly dispersed on MgO for cerium loadings as high as 4 wt%.

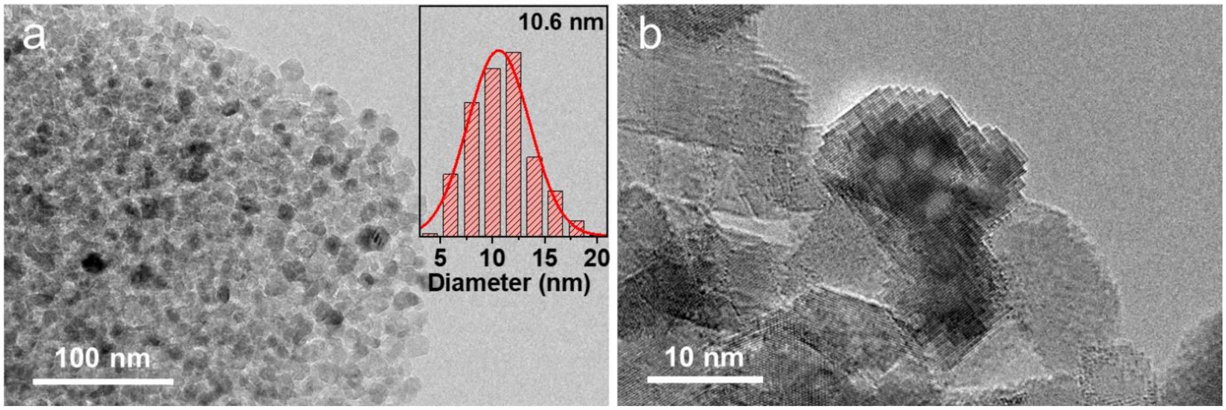

Figure S2. TEM images and particle size distribution plot of Ce-MgO-D(1.6) catalyst.

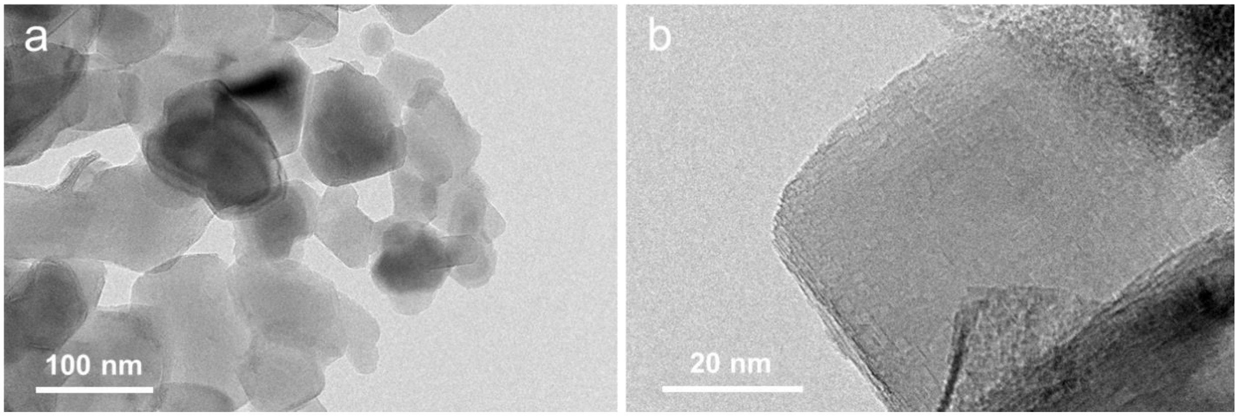

Figure S3. TEM images of MgO-C catalyst.

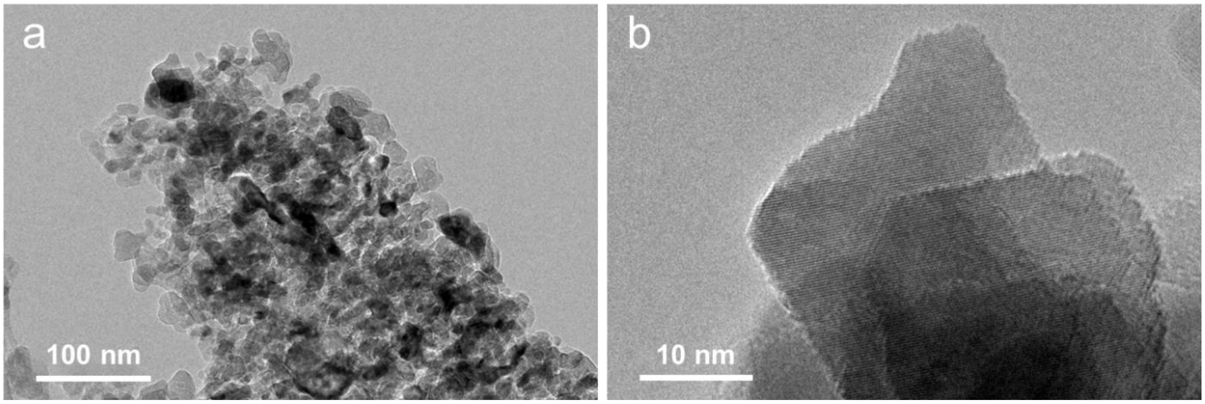

Figure S4. TEM images of MgO-D catalyst.

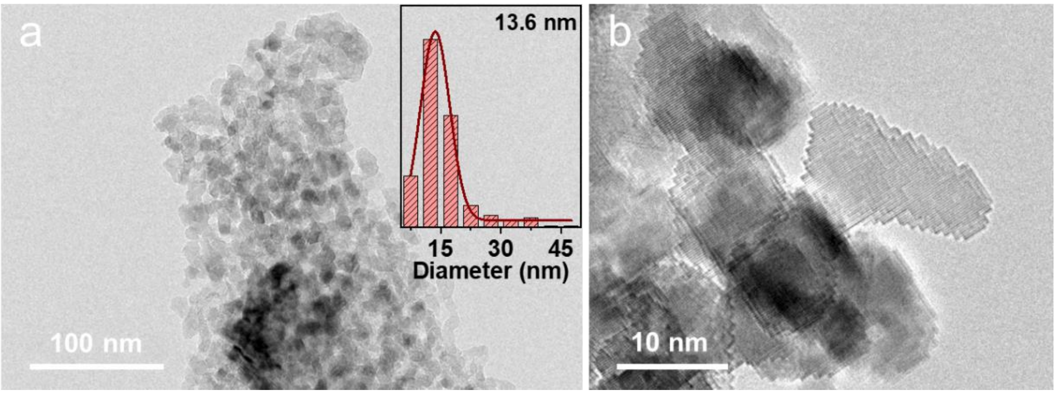

Figure S5. TEM images and particle size distribution plot of Ce-MgO-D(0.4) catalyst.

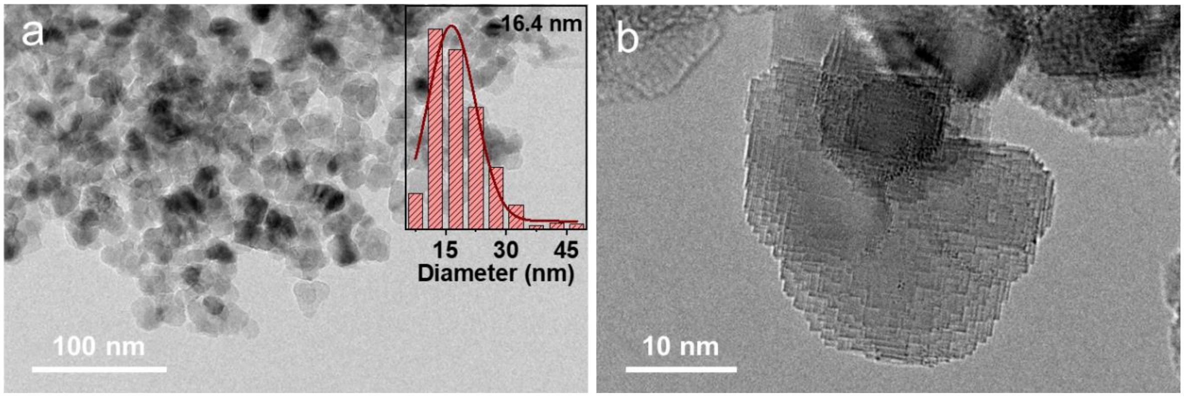

Figure S6. TEM images and particle size distribution plot of Ce-MgO-D(0.8) catalyst.

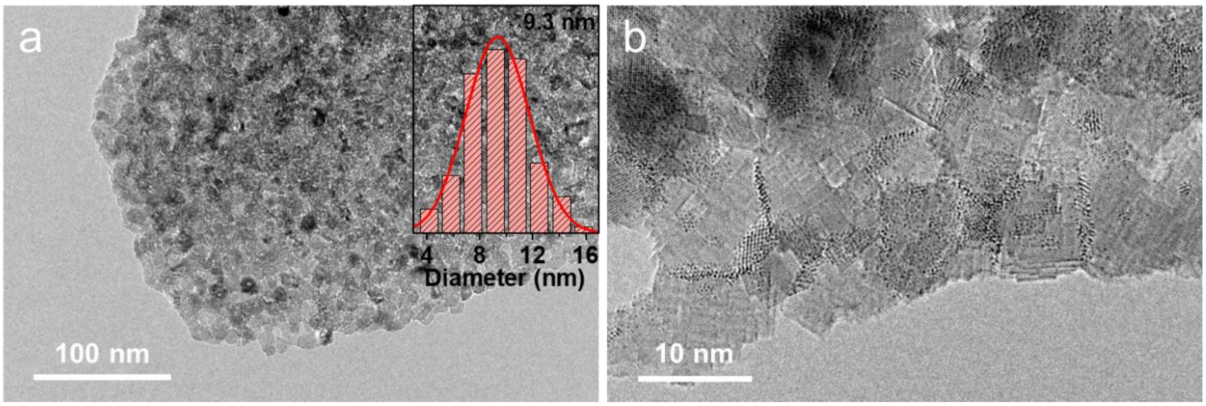

Figure S7. TEM images and particle size distribution plot of Ce-MgO-D(4) catalyst.

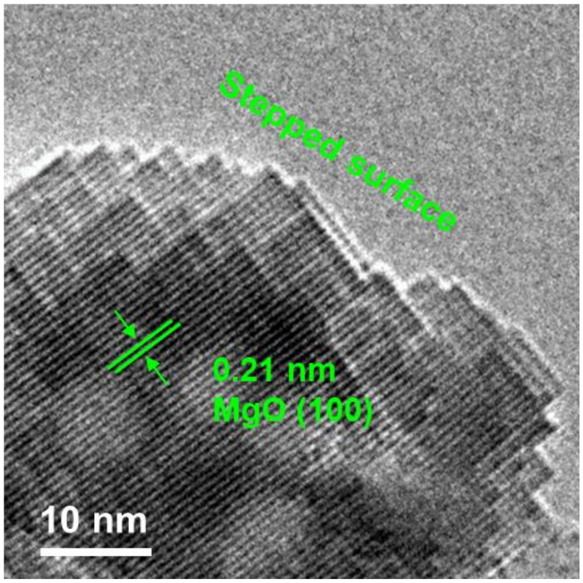

Figure S8. HR-TEM image of Ce-MgO-D(1.6) catalyst.

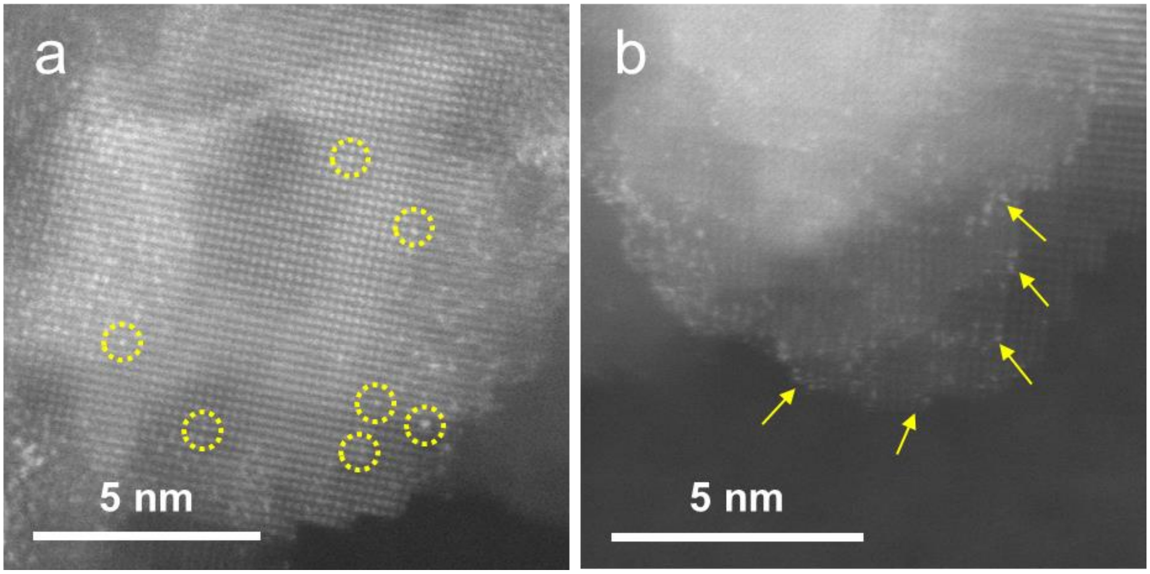

Figure S9. Atomic resolution STEM-ADF images of Ce-MgO-D(1.6) catalyst.

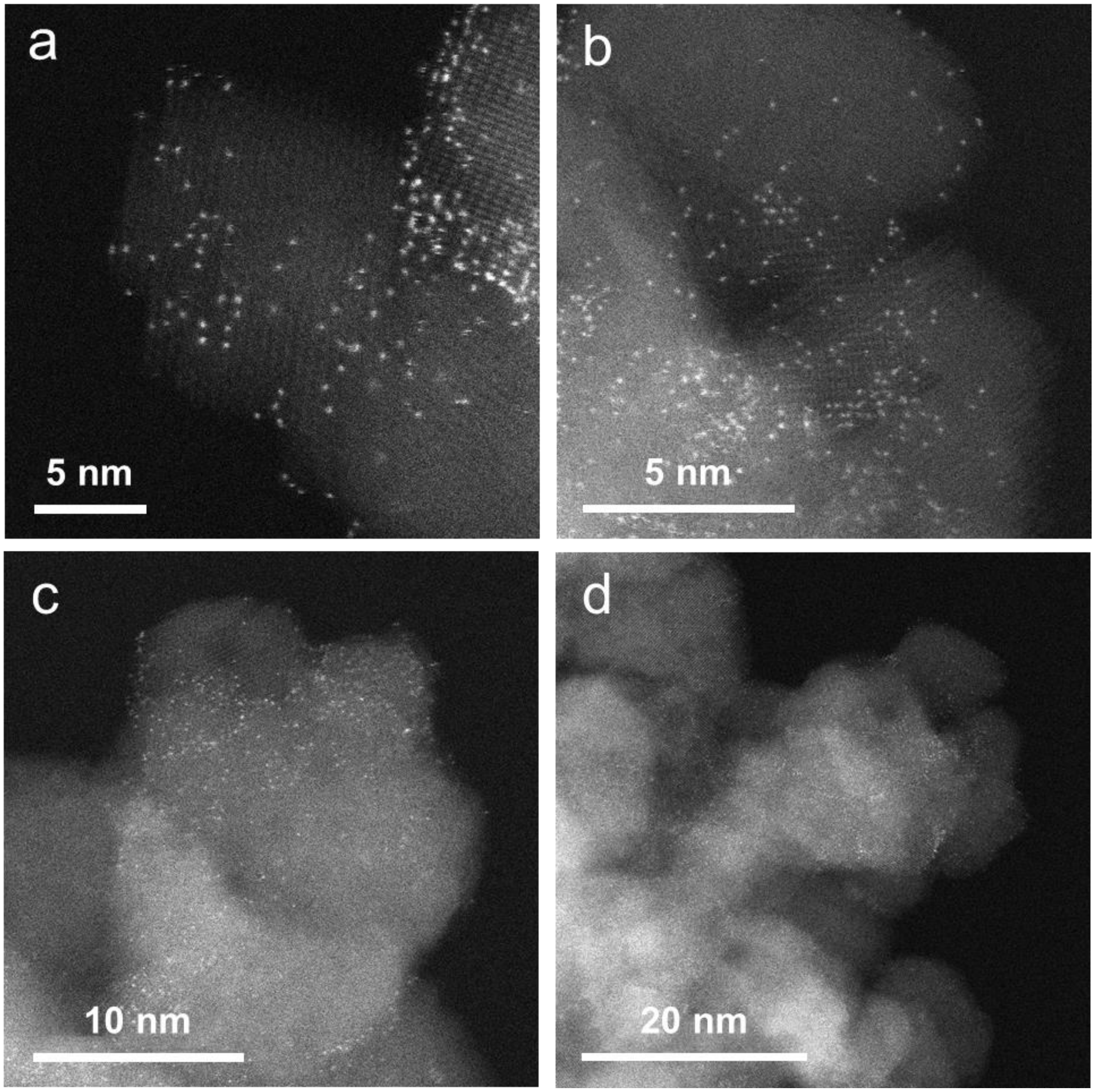

Figure S10. STEM-HAADF images of Ce-MgO-D(1.6) catalyst with different magnifications.

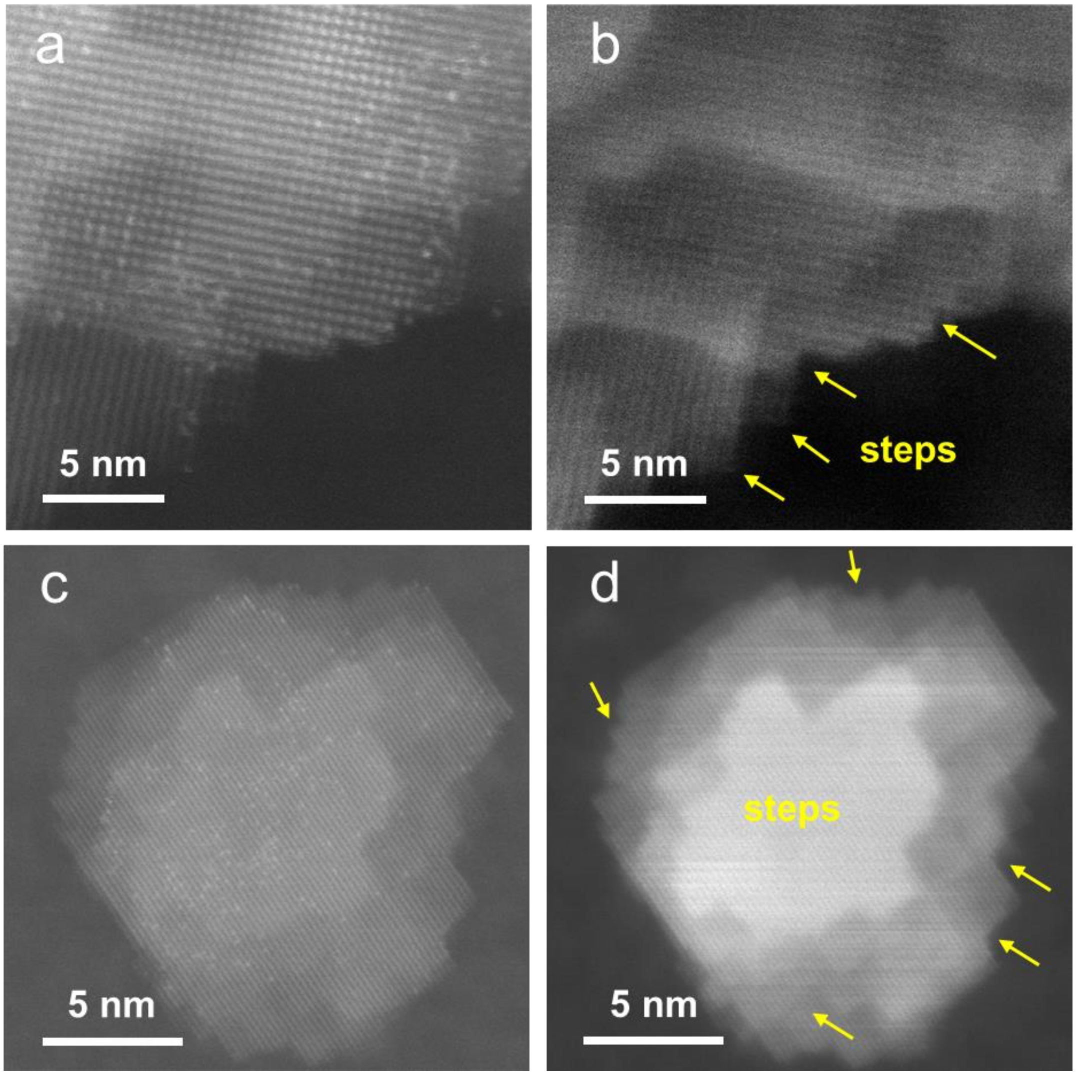

Figure S11. Atomic resolution **a, b)** STEM-ADF images and **c, d)** corresponding STEM-SE images of Ce-MgO-D(1.6) catalyst .

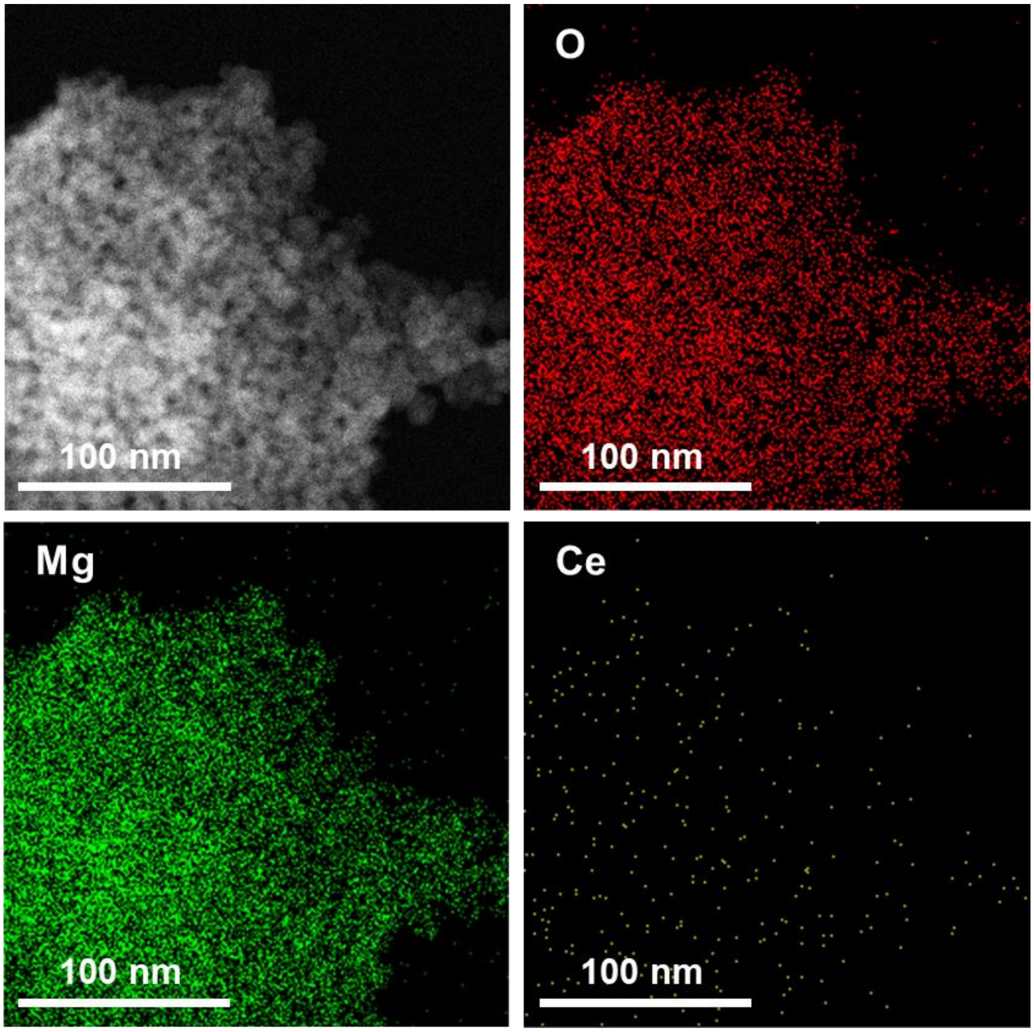

Figure S12. STEM-HAADF image and corresponding EDS elemental mapping (O, Mg, Ce) of Ce-MgO-D(1.6) catalyst.

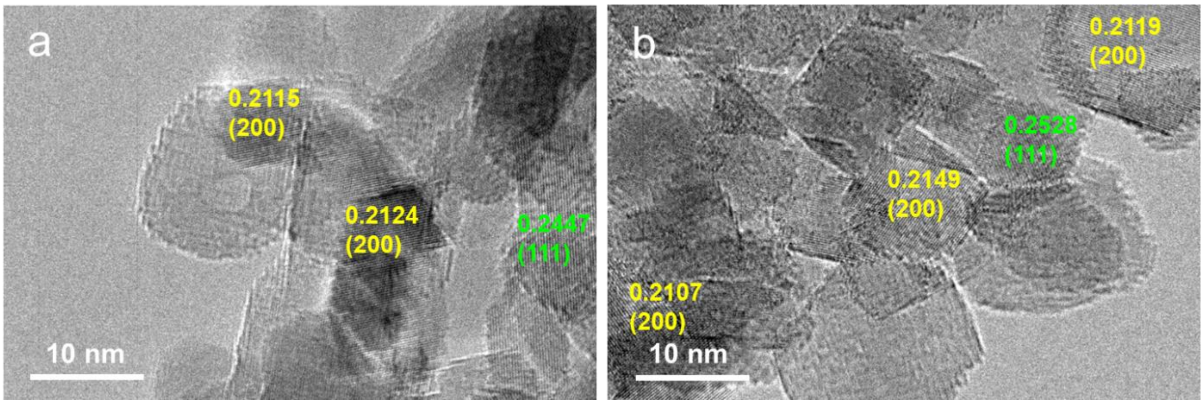

Figure S13. HR-TEM images of **a)** MgO-D and **b)** Ce-MgO-D(1.6) catalysts.

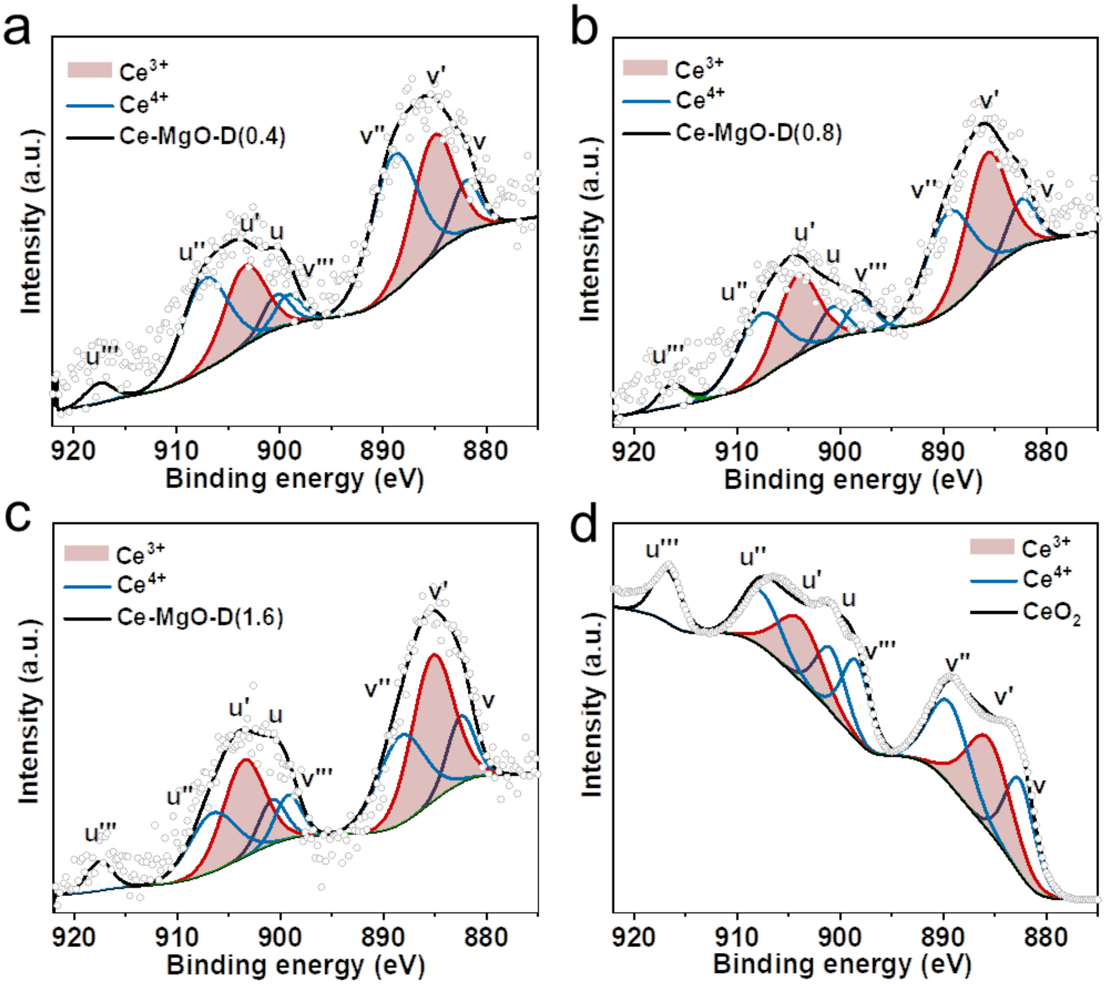

Figure S14. Ce 3d XPS spectra of **a)** Ce-MgO-D(0.4), **b)** Ce-MgO-D(0.8), **c)** Ce-MgO-D(1.6) and **d)** CeO_2 catalysts by XPS.

Table S2. Surface Ce species were analyzed by XPS using different Ce-MgO-D catalysts.

Catalysts	**$Ce^{3+}/(Ce^{3+} + Ce^{4+})$**
Ce-MgO-D(0.4)	36
Ce-MgO-D(0.8)	42
Ce-MgO-D(1.6)	46
CeO_2	33

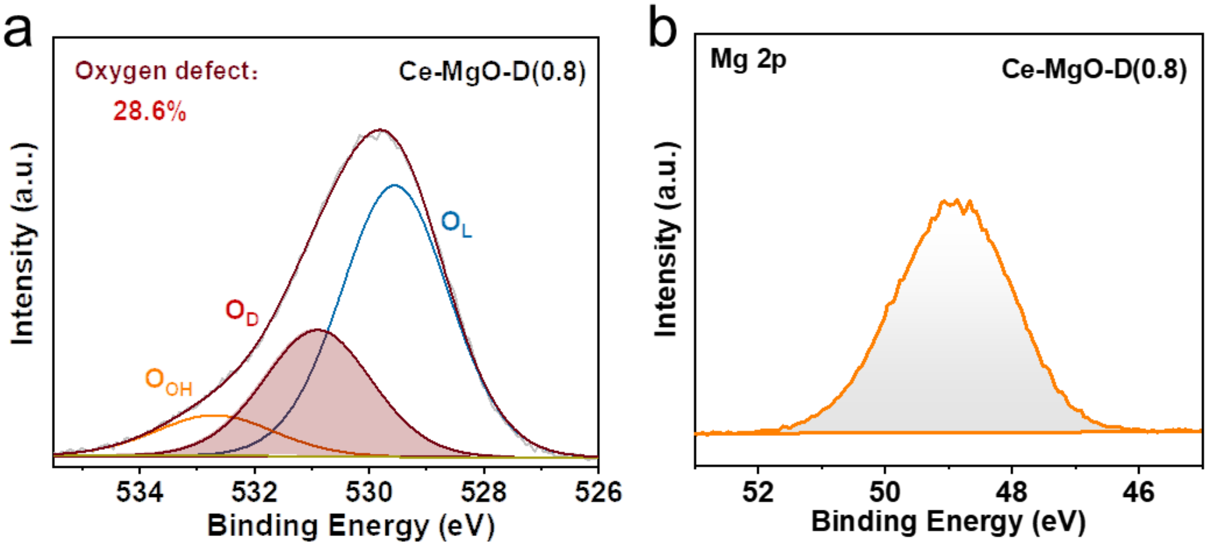

Figure S15. a) O 1s spectra and **b)** Mg 2p spectra of Ce-MgO-D(0.8) catalyst.

Additional catalytic and kinetics data

Table S3. Comparison of reactivity of catalysts in RWGS reaction.

	Catalysts	**T$_{reac.}$, °C**	**GHSV, mL·g$_{cat.}^{-1}$·h^{-1}**	**Conv., %**	**Sel., %**	**Rate, μ mol$_{CO2}$·g$_{cat.}^{-1}$·s^{-1}**	**Rate, mol$_{CO2}$·mol$_{metal}^{-1}$·s^{-1}**	**Ref.**
1	**Ce-MgO-D(1.6)**	600	300,000	9.5	100	84.8	0.74	This work
2	**Ce-MgO-D(1.6)**	600	24,000	52.1	99.9	37.2	0.33	
3	**MgO-D**	600	24,000	36.9	99.9	26.3	—	
4	**MgO-C**	600	24,000	6.5	99.8	4.6	—	
5	**3%Au/CeO$_2$**	500	12,000	30.3	100	22.5	0.15	19
6	**K80-Pt/L**	500	30,000	28.0	100	22.2	1.44	20
8	**Pt/TiO$_2$**	400	6,000	23.0	95.0	20.0	0.39	21
9	**Pt/Al$_2$O$_3$**	400	12,000	20.0	N/A	01.6	0.003	22
10	**Pt/CeO$_2$-IMP-350**	450	72,000	43.0	84.0	62.9	1.40	23
11	**Pt$_{cluster}$/PN-CeO$_2$**	350	12,000	30.1	98.5	48.4	0.26	24
12	**Pt/NR-CeO$_2$**	350	12,000	19.4	100	11.2	0.17	24
13	**Pt/mullite**	550	30,000	22.9	83.9	38.34	0.37	25
14	**K-Pt/mullite**	550	30,000	30.9	99.2	51.73	0.50	25
15	**Pt/SiO$_2$@CNT**	500	—	4	98.5	7.4	0.33	26
16	**0.5%Pd/La$_2$O$_3$/MWCNT**	400	72,000	20.0	100	42.9	0.86	27
17	**Pd-In/SiO$_2$**	600	60,000	9.57	100	14.24	0.05	28
18	**Pd/SiO$_2$**	600	60,000	29.39	83	43.74	0.15	28
19	**Ru(col)/ZrTiO$_4$**	477	—	26.0	92.0	57.6	0.33	29
20	**1%Ni/CeO$_2$**	400	120,000	4.5	90.0	33.5	0.20	30
21	**Ni-Mo/Al$_2$O$_3$**	600	30,000	35.0	N/A	65.1	0.07	31
22	**10%Cu-0.3%Fe/SiO$_2$**	600	120,000	12.0	100	89.3	0.06	32
23	**10%Cu/SiO$_2$**	600	120,000	8.0	100	59.5	0.04	32
24	**0.3%Fe/SiO$_2$**	600	120,000	2.0	100	14.9	0.28	32
25	**1%NiO/CeO$_2$/SBA-15**	450	1500	2.5	100	0.2	0.001	33
26	**5%Co-N-C**	500	6,000	52.4	96.0	7.0	0.008	34

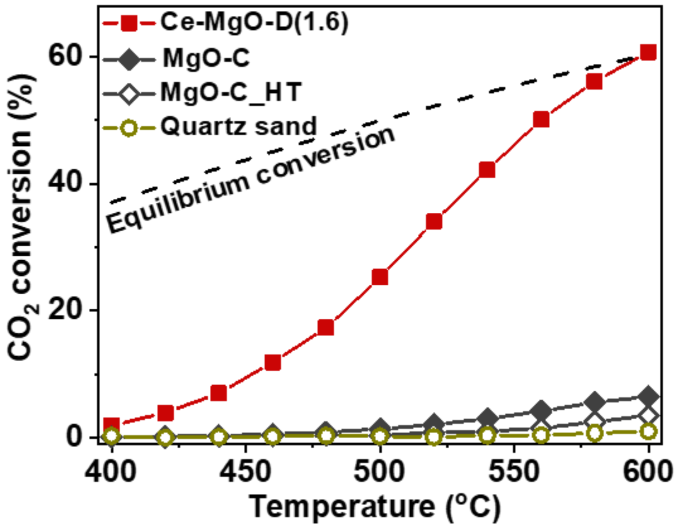

Figure S16. Catalytic activity of Ce-MgO-D(1.6) catalyst. Reaction conditions: CO_2/H_2=1/3, GHSV = 4800 mL·g_{cat}^{-1}·h^{-1}. Catalytic activity of quartz sand, MgO-C and MgO-C_HT catalyst (HT refers to catalysts treated at 1200 °C high temperature). Reaction conditions: CO_2/H_2=1/3, GHSV = 24,000 mL·g_{cat}^{-1}·h^{-1}.

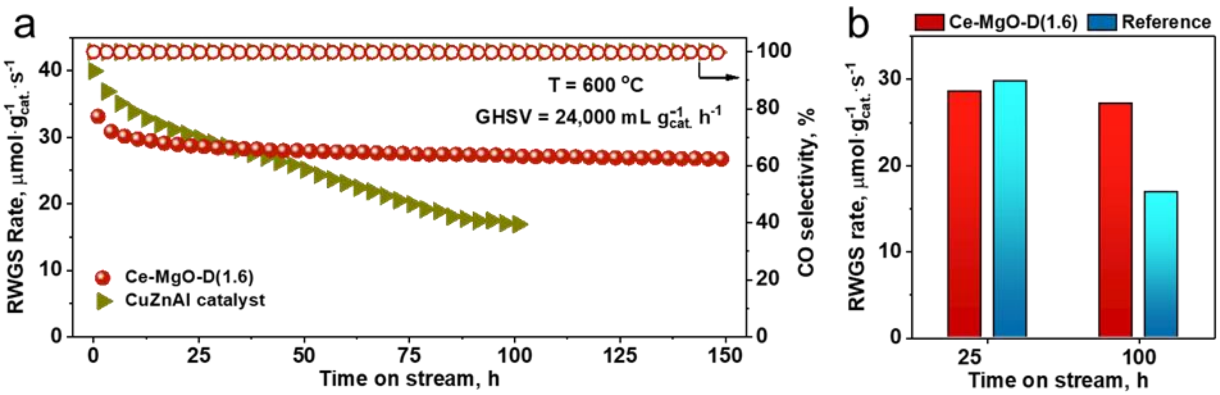

Figure S17. a) Long-term catalytic tests of the Ce-MgO-D(1.6) and the reference (commercial) CuZnAl syngas catalyst. **b)** Catalytic tests of the Ce-MgO-D(1.6) compared to a reference (commercial) CuZnAl syngas catalyst (comparison of RWGS rate after 25 and 100 h of time on stream, 600 °C, GHSV = 24,000 mL·g$_{cat}^{-1}$·h^{-1}).

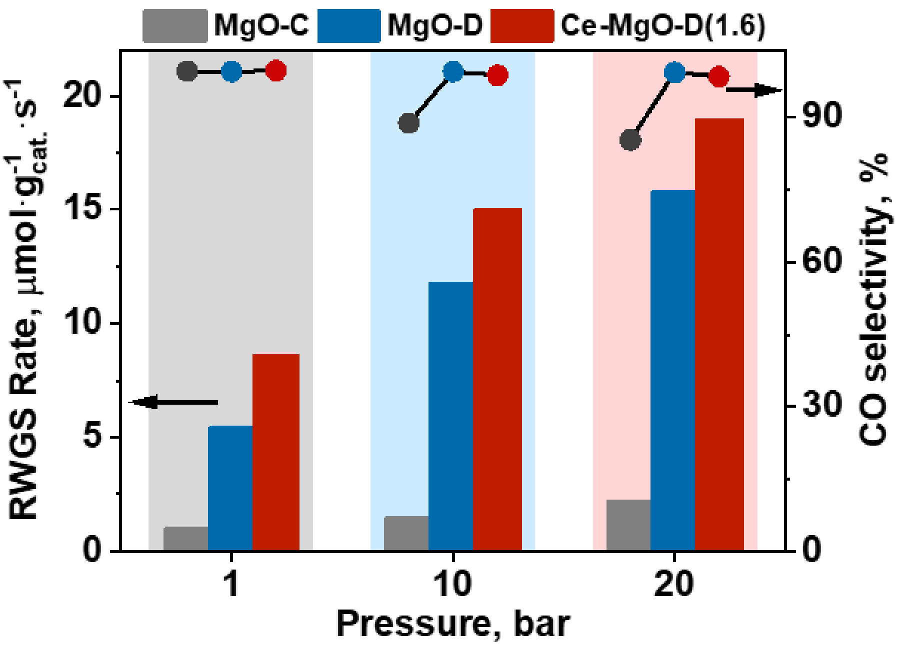

Figure S18. RWGS reaction activity of MgO-C, MgO-D and Ce-MgO-D(1.6) at 500 °C as a function of pressure.

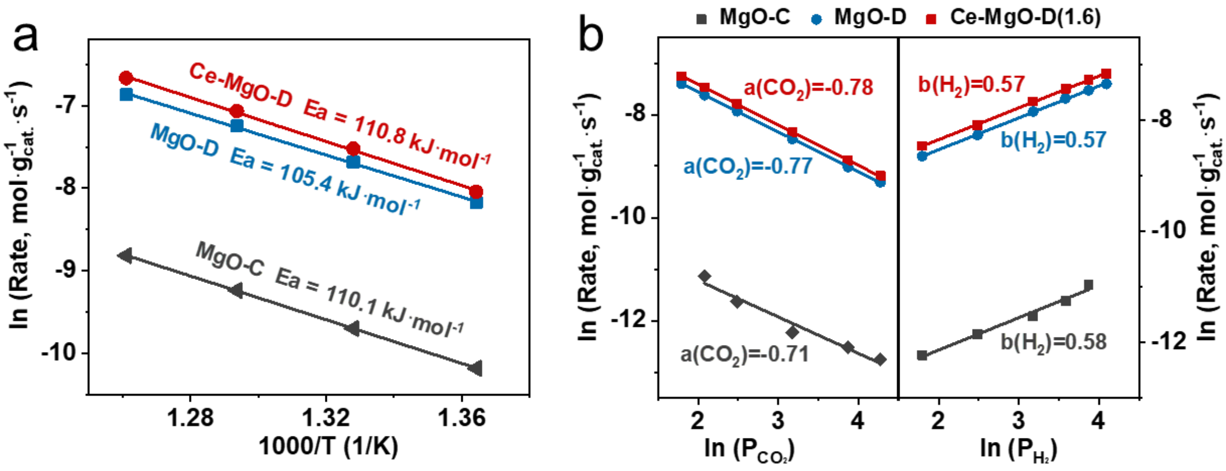

Figure S19. a) Apparent activation energy value of MgO-C, MgO-D and Ce-MgO-D(1.6) catalysts. **b)** Effect of CO_2 (left) and H_2 (right) partial pressure on reaction rate of MgO-C, MgO-D and Ce-MgO-D(1.6) catalysts at 500 °C.

Table S4. Kinetic results of MgO-C, MgO-D and Ce-MgO-D(1.6) catalysts.

$R=k_{app}[CO_2]^a[H_2]^b$				
Catalysts	$k_{app}/\times10^{-5}$	a	b	Ea, $kJ\cdot mol^{-1}$
MgO-C	0.5	-0.71	0.58	110.1
MgO-D	17.2	-0.77	0.57	105.4
Ce-MgO-D(1.6)	20.3	-0.78	0.57	110.8

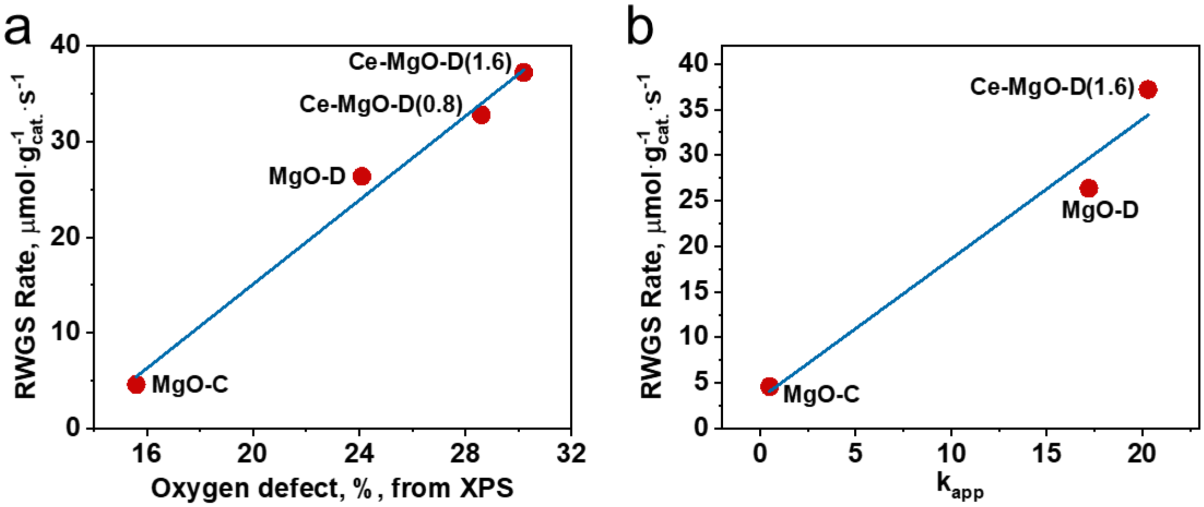

Figure S20. Correlation between the catalytic performance in RWGS with **a)** oxygen defects, and **b)** rate constant k_{app} over MgO-C, MgO-D, and Ce-MgO-D catalysts.

FT-IR additional results

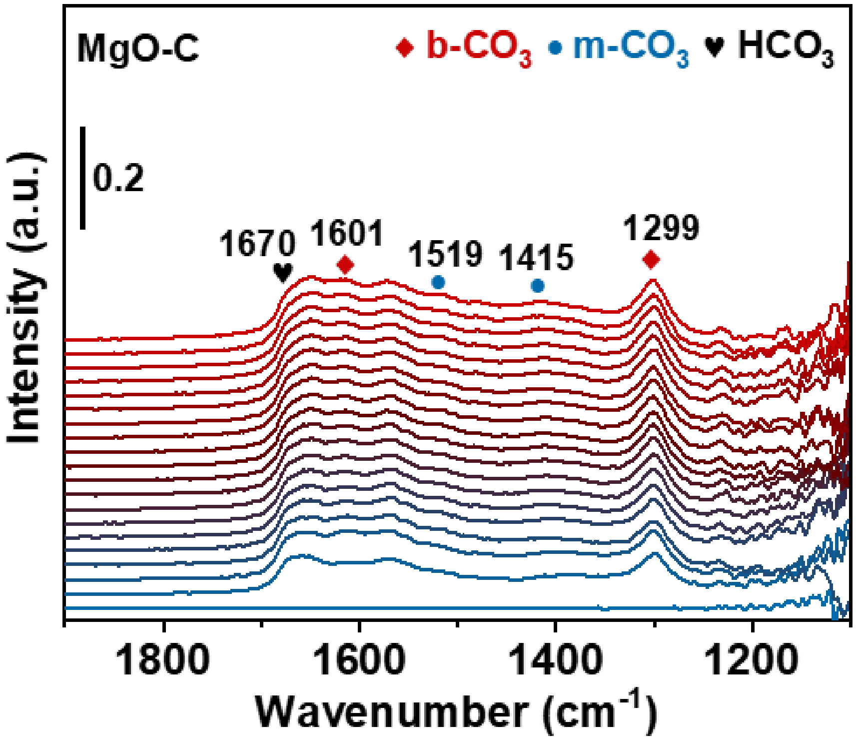

Figure S21. Operando DRIFT spectra taken for MgO-C catalysts at 0.1MPa CO$_2$ at 350 °C. Spectra referenced to different catalysts under 0.1 MPa Ar at 350 °C.

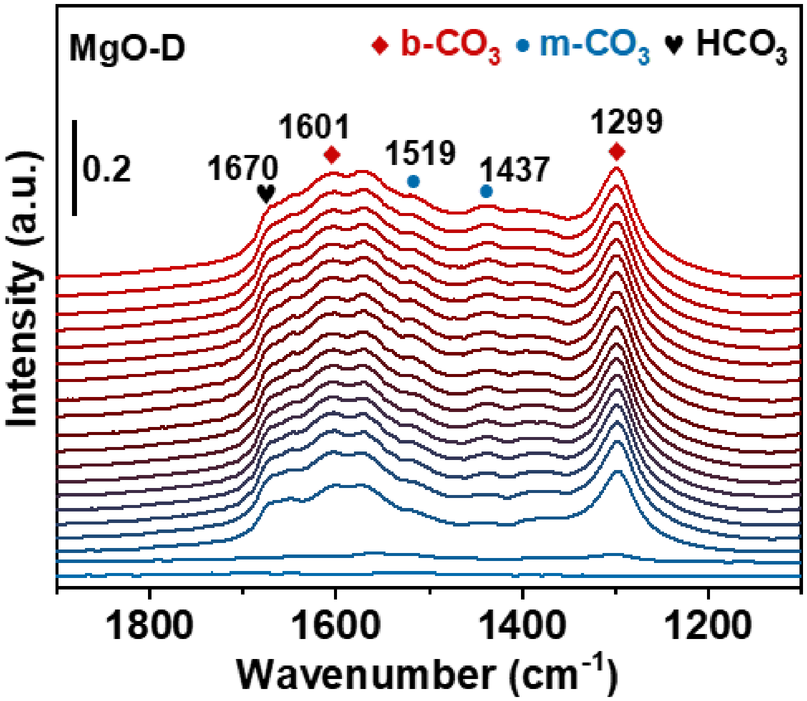

Figure S22. Operando DRIFT spectra taken for MgO-D catalysts at 0.1MPa CO_2 at 350 °C. Spectra referenced to different catalysts under 0.1 MPa Ar at 350 °C.

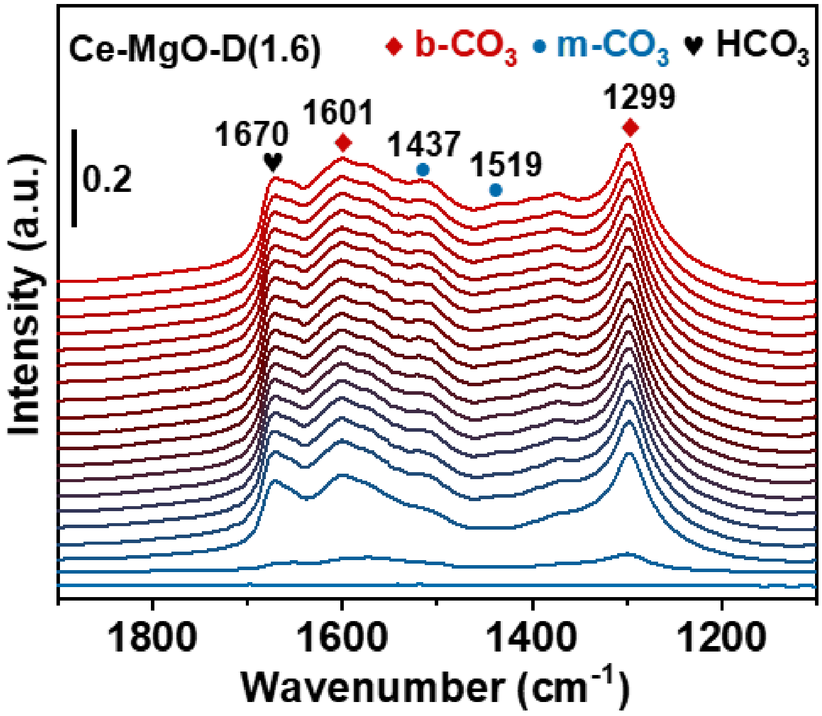

Figure S23. Operando DRIFT spectra taken for Ce-MgO-D(1.6) catalysts at 0.1MPa CO_2 at 350 °C. Spectra referenced to different catalysts under 0.1 MPa Ar at 350 °C.

Additional Theoretical calculations data

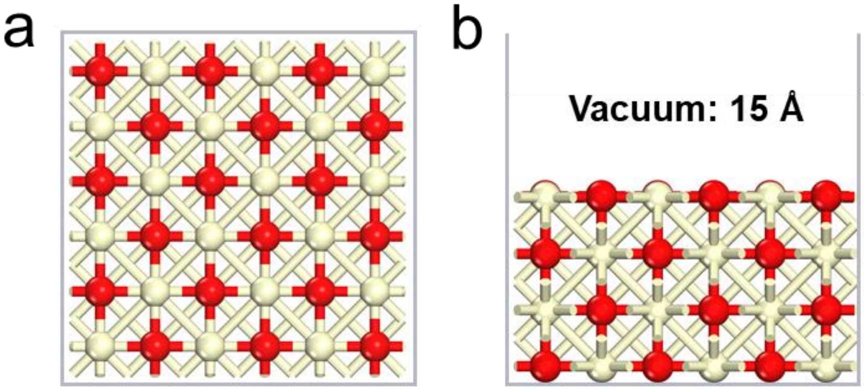

Figure S24. a) Top and **b)** side views of the optimized MgO(100) model. The red and yellow spheres represent O and Mg atoms, respectively.

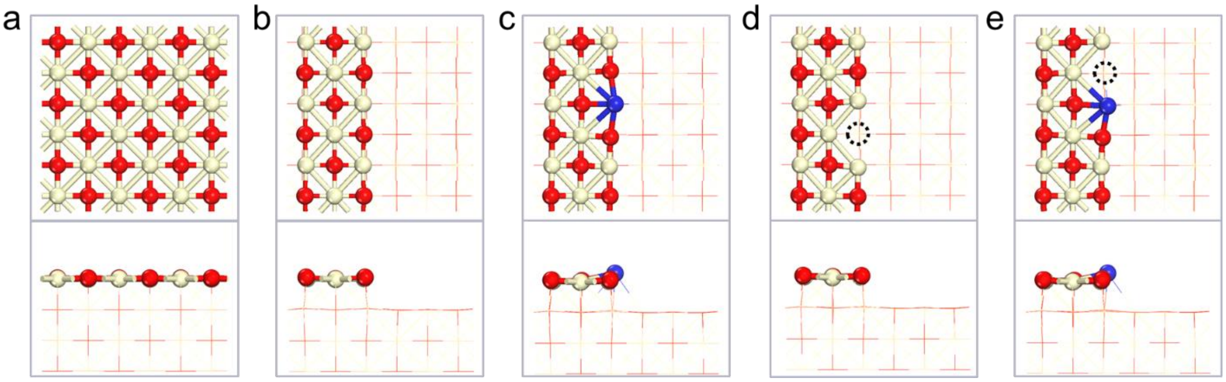

Figure S25. The structure models of **a)** MgO, **b)** MgO-D, **c)** Ce-MgO-D, **d)** O_v-MgO-D and **e)** Ce-O_v-MgO-D catalysts. In the top view, atoms from the second layer to the bottom are depicted in a line style to enhance the visualization of the surface layer. Yellow: Mg, blue: Ce, red: O, black dashed circle: oxygen vacancy.

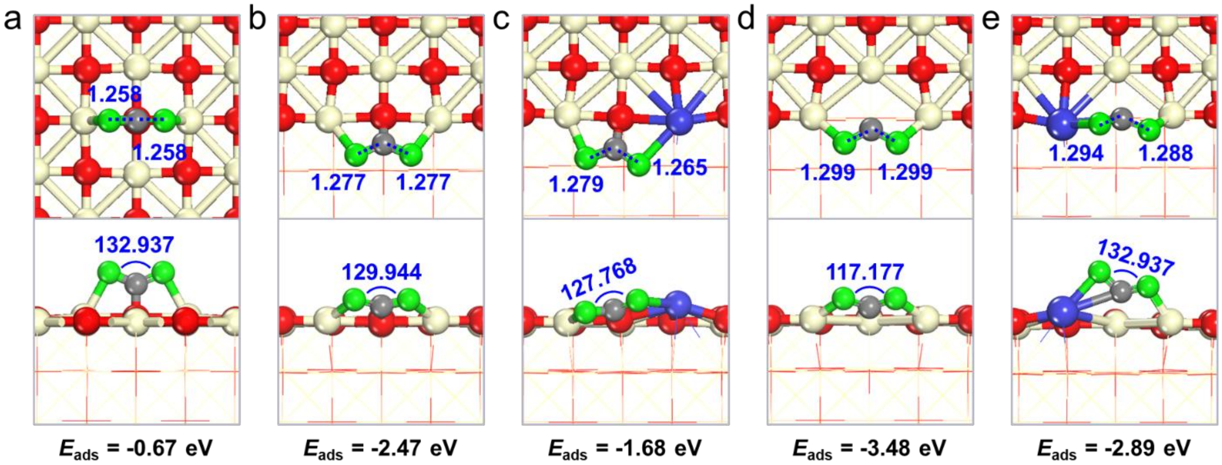

Figure S26. Top and side views of the optimized geometries and calculated adsorption energies (E_{ads}) of CO_2 on the models of **a)** MgO, **b)** MgO-D, **c)** Ce-MgO-D, **d)** O_v-MgO-D and **e)** Ce-O_v-MgO-D catalysts, respectively. The red, green, grey, yellow and blue spheres represent O, O, C, Mg and Ce atoms, respectively. Distances between C atoms and O atoms are in angstroms (Å), and the bending angle of CO_2 molecule are indicated in degrees (°).

Table S5. The adsorption energy (eV) of CO_2 and H_2 on different models.

Catalysts	**CO_2 E_{ads}/(eV)**	**H_2 E_{ads}/(eV)**
MgO	-0.67	-0.13
MgO-D	-2.47	-0.25
Ce-MgO-D	-1.68	—
O_v-MgO-D	-3.48	-0.13
Ce-O_v-MgO-D	-2.89	—

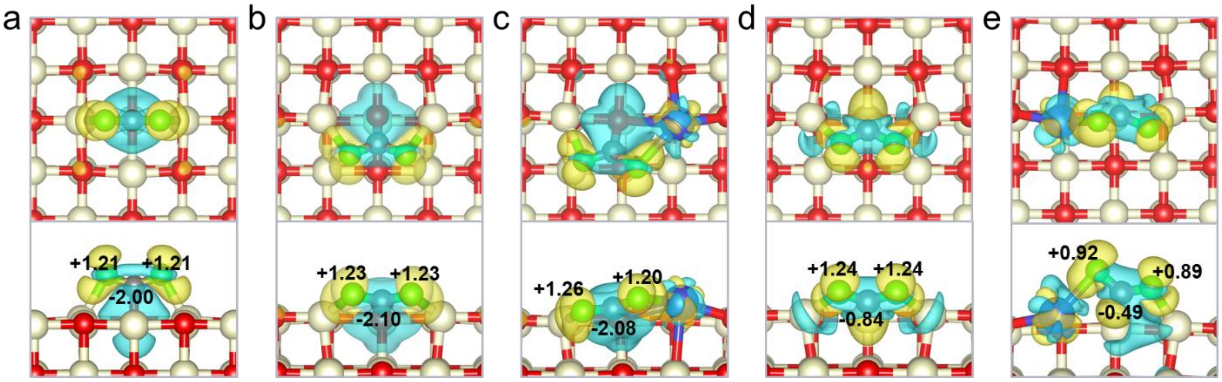

Figure S27. Differential charge density and Bader charge of **a)** MgO, **b)** MgO-D, **c)** Ce-MgO-D, **d)** O_v-MgO-D and **e)** Ce-O_v-MgO-D surfaces, and the cyan and yellow regions represent the charge depletion and accumulation, respectively. The isosurface value is 0.003 e/Bohr^3. The red, green, grey, yellow and blue spheres represent O, O, C, Mg and Ce atoms, respectively.

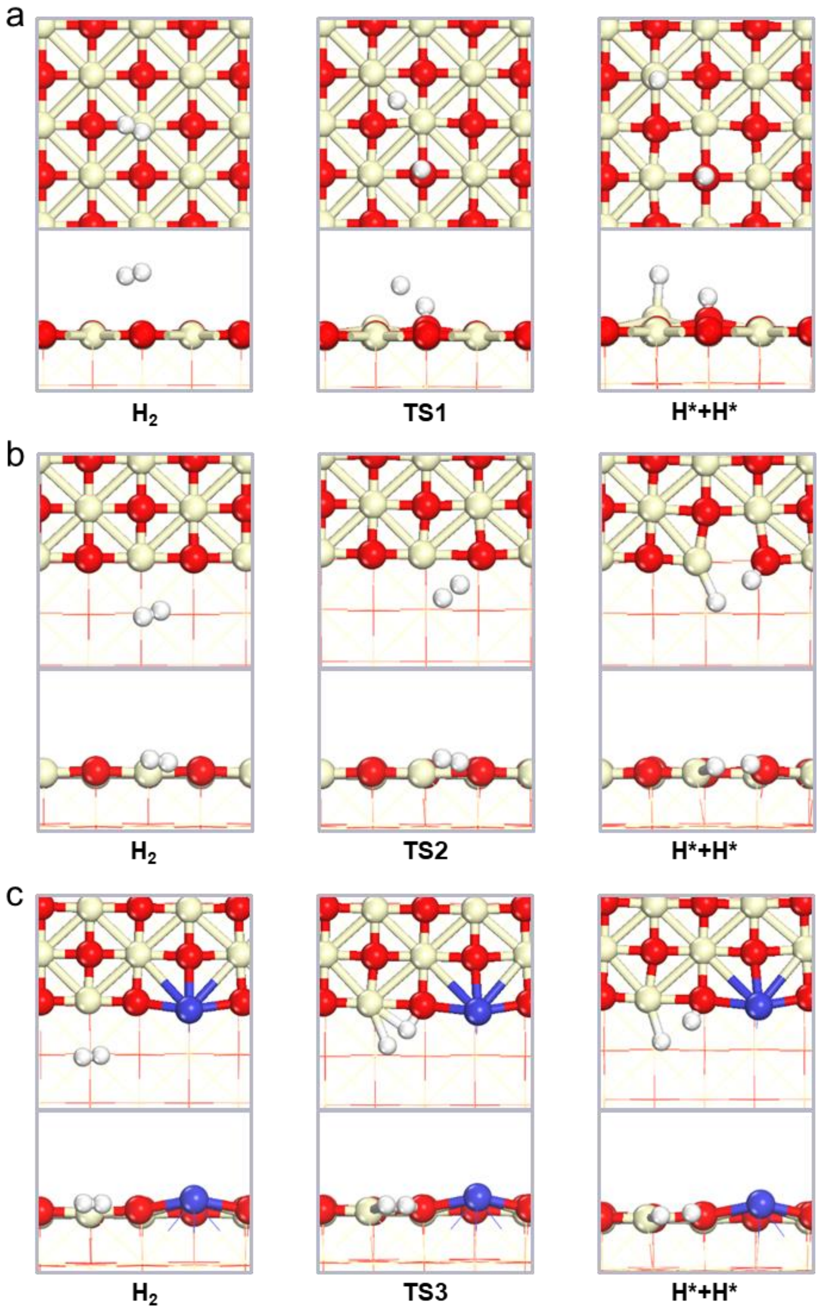

Figure S28. The structures of initial state, transition state and final state involved in the dissociation of H_2 on the models of **a)** MgO, **b)** MgO-D and **c)** Ce-MgO-D catalysts. The red, white, yellow and blue spheres represent O, H, Mg and Ce atoms, respectively.

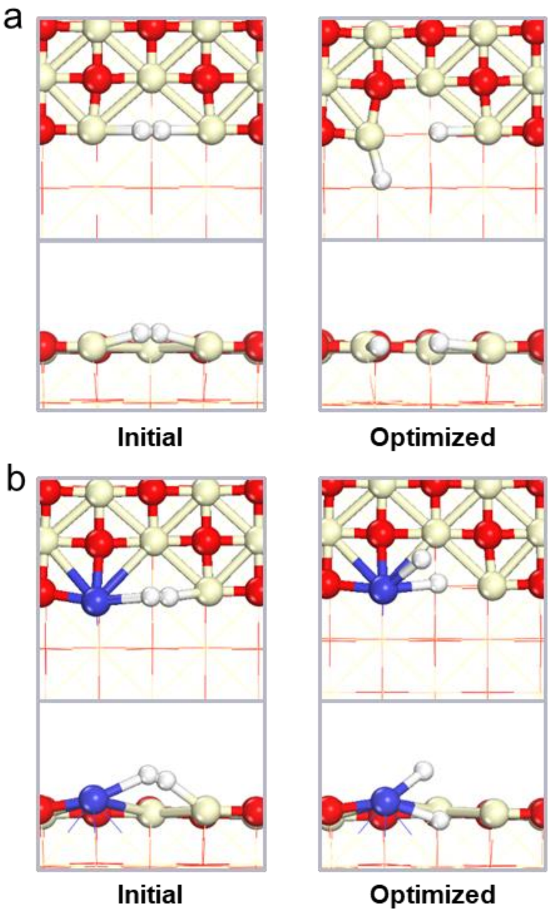

Figure S29. The optimized structures of H_2 adsorption configurations on the models of **a)** O_v-MgO-D and **b)** Ce-O_v-MgO-D catalysts. The red, white, yellow and blue spheres represent O, H, Mg and Ce atoms, respectively.

<u>Other additional results</u>

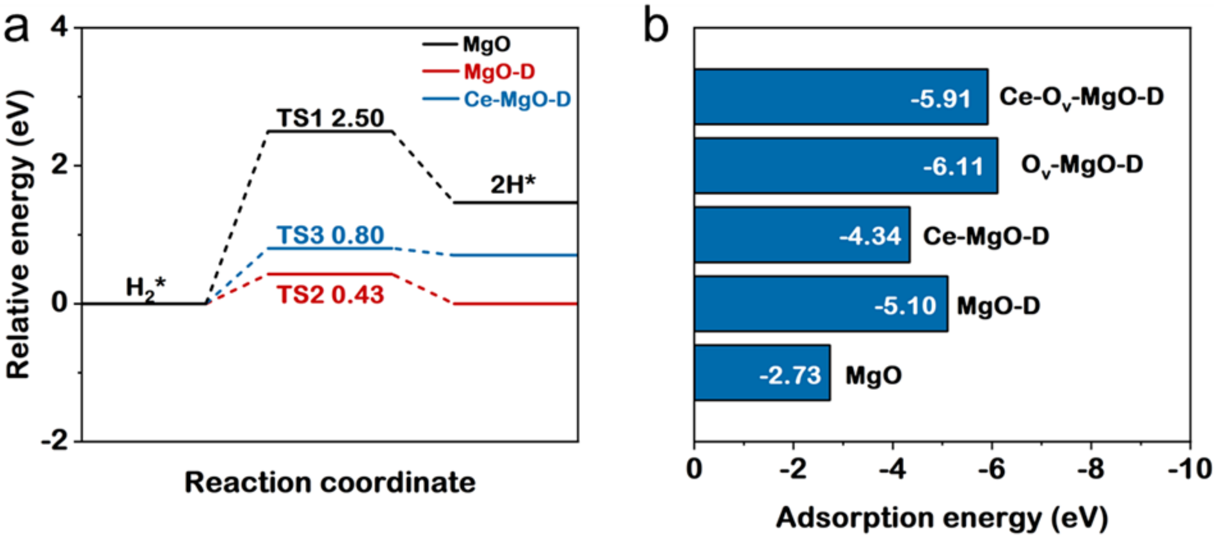

Figure S30. a) Energy profiles of H_2 dissociation on the MgO, MgO-D and Ce-MgO-D models. **b)** Co-adsorption energy of the dissociated two H atoms on the models of MgO, MgO-D, Ce-MgO-D, O_v-MgO-D and Ce-O_v-MgO-D catalysts.

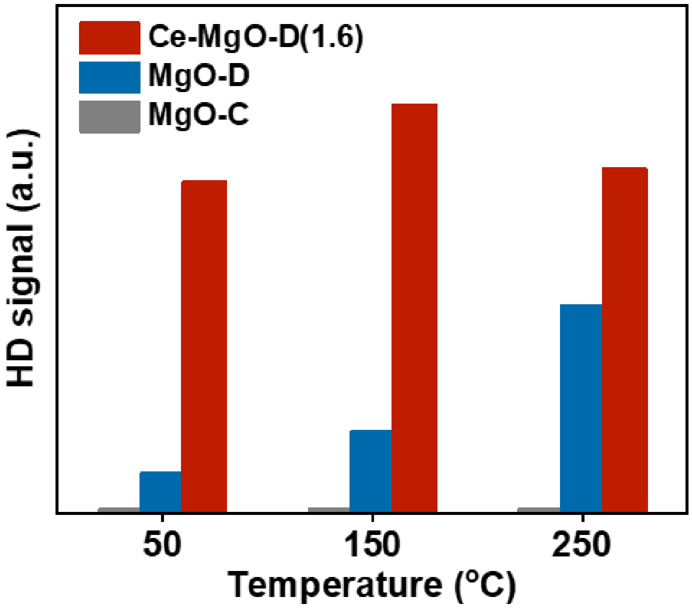

Figure S31. H_2-D_2 exchange reaction on MgO-C, MgO-D and Ce-MgO-D(1.6).

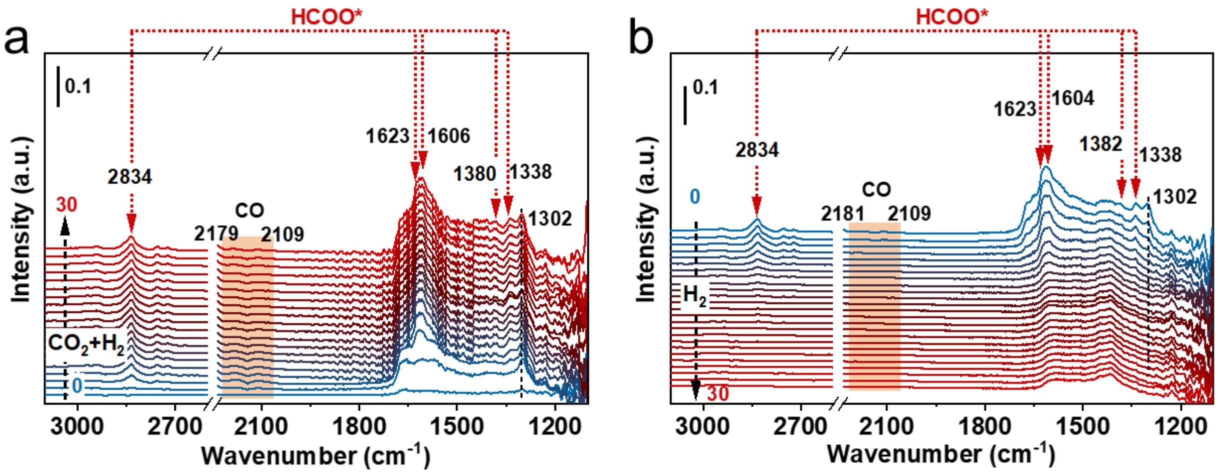

Figure S32. a) In-situ DRIFT spectra taken for MgO-C catalysts at 0.1MPa CO_2:H_2=1:3 at 450 °C. **b)** In-situ DRIFTs of MgO-C pre-reacted at 450 °C for 40 min under CO_2:H_2=1:3 atmosphere followed by H_2 for 30 min. Spectra referenced to different catalysts under 0.1 MPa Ar at 450 °C.

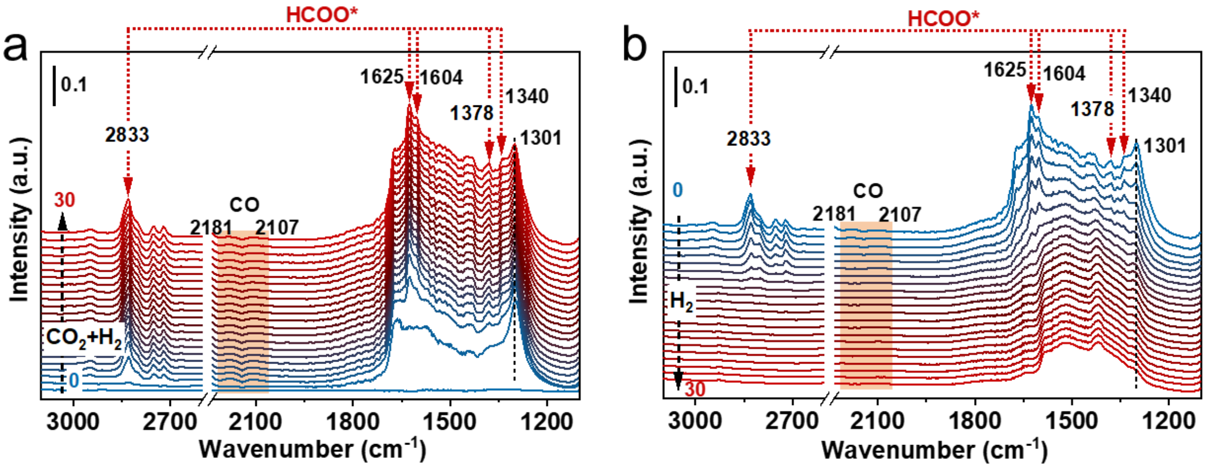

Figure S33. a) In-situ DRIFT spectra taken for MgO-D catalysts at 0.1 MPa CO_2:H_2=1:3 at 450 °C. **b)** In-situ DRIFTs of MgO-D pre-reacted at 450 °C for 40 min under CO_2:H_2=1:3 atmosphere followed by H_2 for 30 min. Spectra referenced to different catalysts under 0.1 MPa Ar at 450 °C.

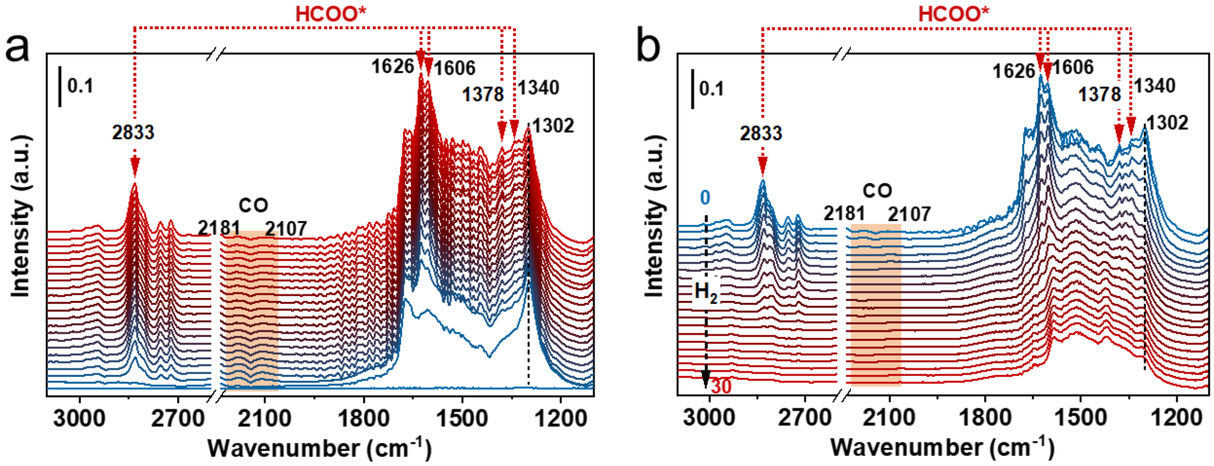

Figure S34. a) In-situ DRIFT spectra taken for Ce-MgO-D(1.6) catalysts at 0.1MPa CO_2:H_2=1:3 at 450 °C. **b)** In-situ DRIFTs of Ce-MgO-D pre-reacted at 450 °C for 40 min under CO_2:H_2=1:3 atmosphere followed by H_2 for 30 min. Spectra referenced to different catalysts under 0.1 MPa Ar at 450 °C.

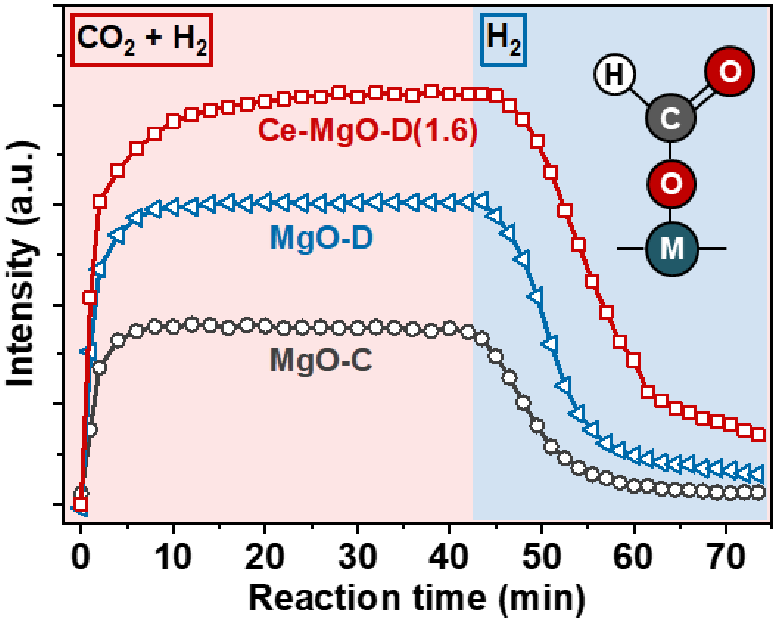

Figure S35. The corresponding quantitative surface formate (HCOO*, 1606 cm^{-1}) from in-situ DRIFTs of MgO-C, MgO-D and Ce-MgO-D(1.6) catalysts during CO_2:H_2=1:3 atmosphere switch to H_2 at 450 °C.

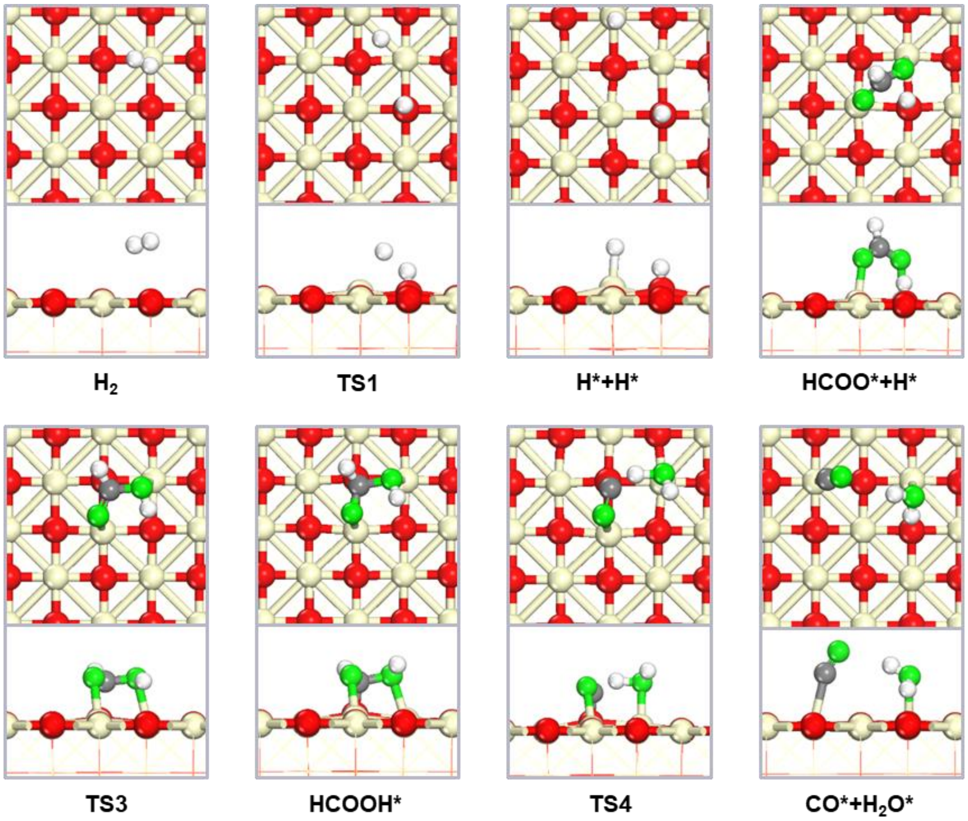

Figure S36. The structures of initial state, transition state and final state involved in CO_2 hydrogenation to CO on the MgO surface. The red, white, grey, green and yellow spheres represent O, H, C, O and Mg atoms, respectively.

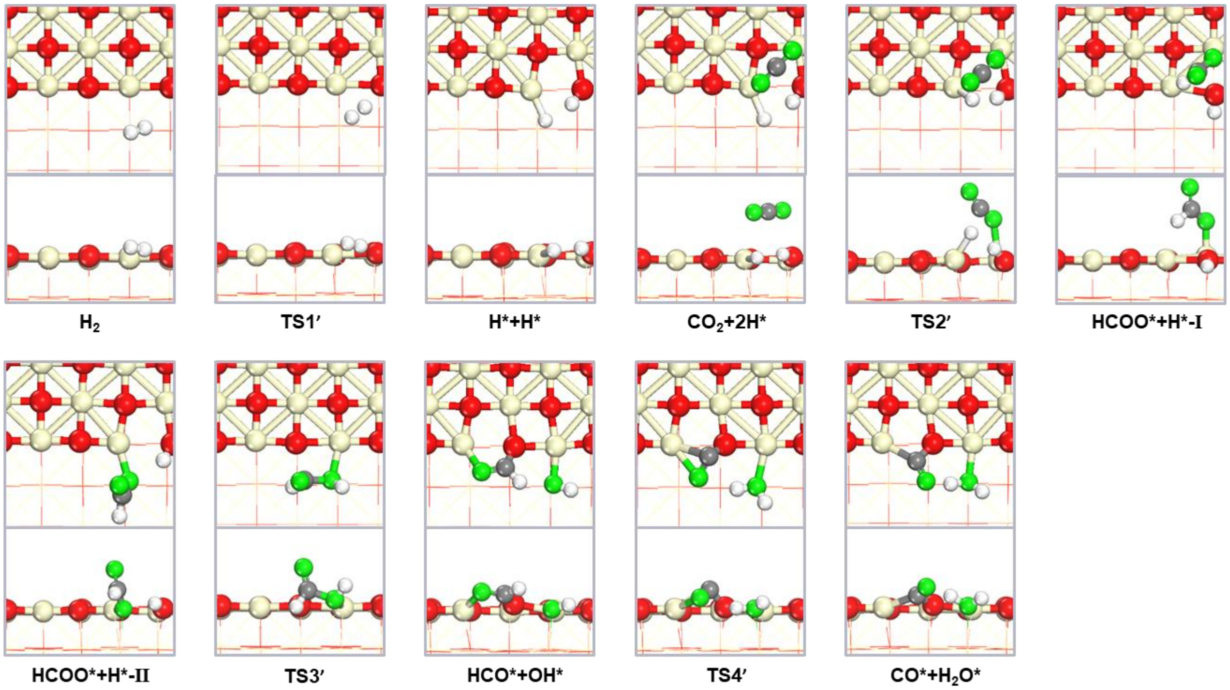

Figure S37. The structures of the initial state, transition state and final state involved in CO_2 hydrogenation to CO on the MgO-D surface. The red, white, grey, green and yellow spheres represent O, H, C, O and Mg atoms, respectively.

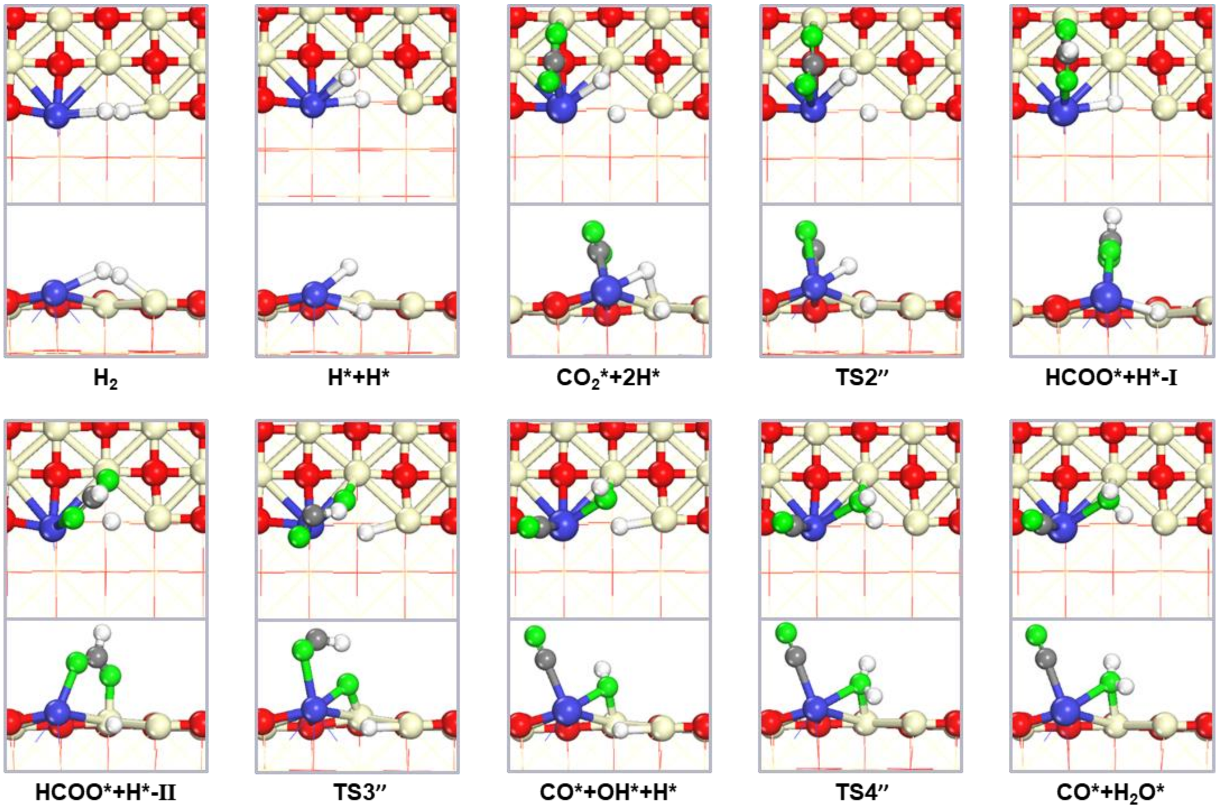

H_2 H*+H* CO_2*+2H* TS2″ HCOO*+H*-I

HCOO*+H*-II TS3″ CO*+OH*+H* TS4″ CO*+H_2O*

Figure S38. The structures of initial state, transition state and final state involved in CO_2 hydrogenation to CO on the Ce-O_v-MgO-D surface. The red, white, grey, green and yellow spheres represent O, H, C, O and Mg atoms, respectively.

Table S6. Activation free energy (Ga/eV) and reaction free energy (ΔG/eV) of elementary steps involving in RWGS reaction over MgO, MgO-D and Ce-O$_v$-MgO-D catalyst at 873.15 K.

Catalysts	**Elementary step reaction**	**G_a (eV)**	**ΔG (eV)**
MgO	H_2*→H*+H*	2.50	1.47
	CO_2+2H*→HCOO*+H*	-	-3.07
	HCOO*+H*→HCOOH*+*	1.39	1.17
	HCOOH *+*→CO*+H_2O*	0.97	-0.03
	CO*+H_2O*→CO+H_2O*+*	-	-1.22
	CO+H_2O*+*→CO+H_2O+2*	-	-0.54
MgO-D	H_2*→H*+H*	0.43	0.00
	CO_2*+2H*→HCOO*+H*-I	0.43	-0.01
	HCOO*+H*-I→HCOO*+H*-II	-	-1.31
	HCOO*+H*-II→HCO*+OH*	1.77	-0.14
	HCO*+OH*→CO*+H_2O*	2.15	0.89
	CO*+H_2O*→CO*+H_2O+*	-	0.02
	CO*+H_2O+*→CO+H_2O+2*	-	-0.47
Ce-O$_v$-MgO-D	H_2*→H*+H*	-	-1.18
	CO_2*+2H*→HCOO*+H*-I	0.29	0.25
	HCOO*+H*-I→HCOO*+H*-II	-	-0.28
	HCOO*+H*-II+*→CO*+OH*+H*	2.29	0.87
	CO*+OH*+H*→CO*+H_2O*+*	1.79	1.74
	CO*+H_2O*→CO*+H_2O+*	-	-0.50
	CO*+H_2O+*→CO+H_2O+2*	-	-0.19

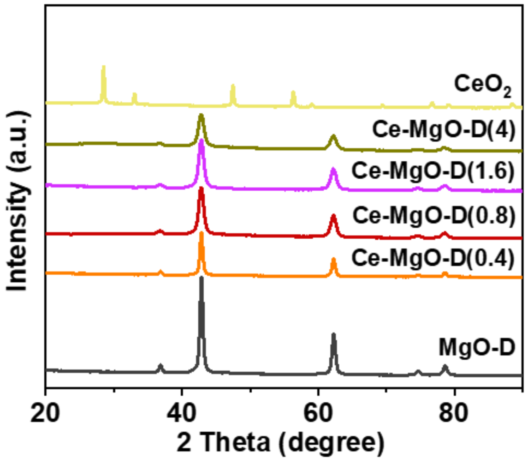

Figure S39. XRD patterns for spent Ce-MgO-D catalysts with different Ce content after the reaction.

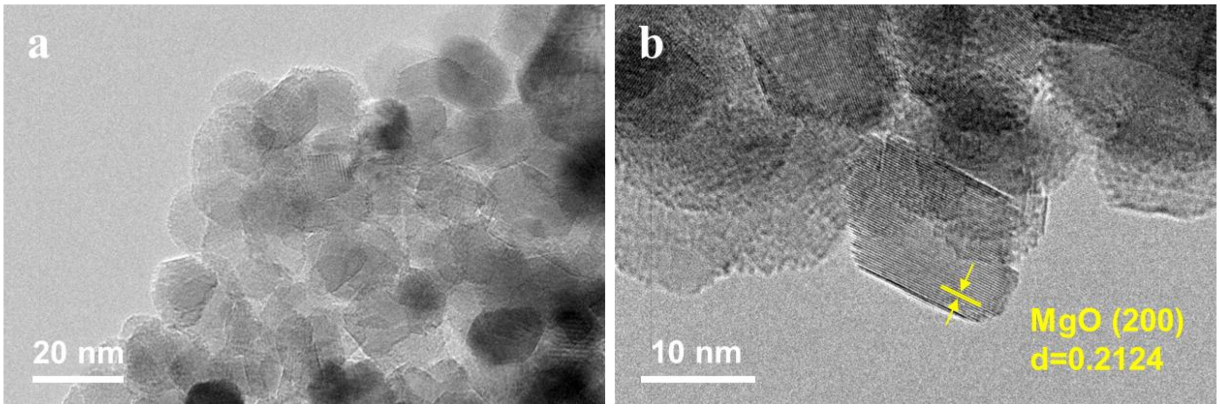

Figure S40. HR-TEM images of spent Ce-MgO-D(1.6).

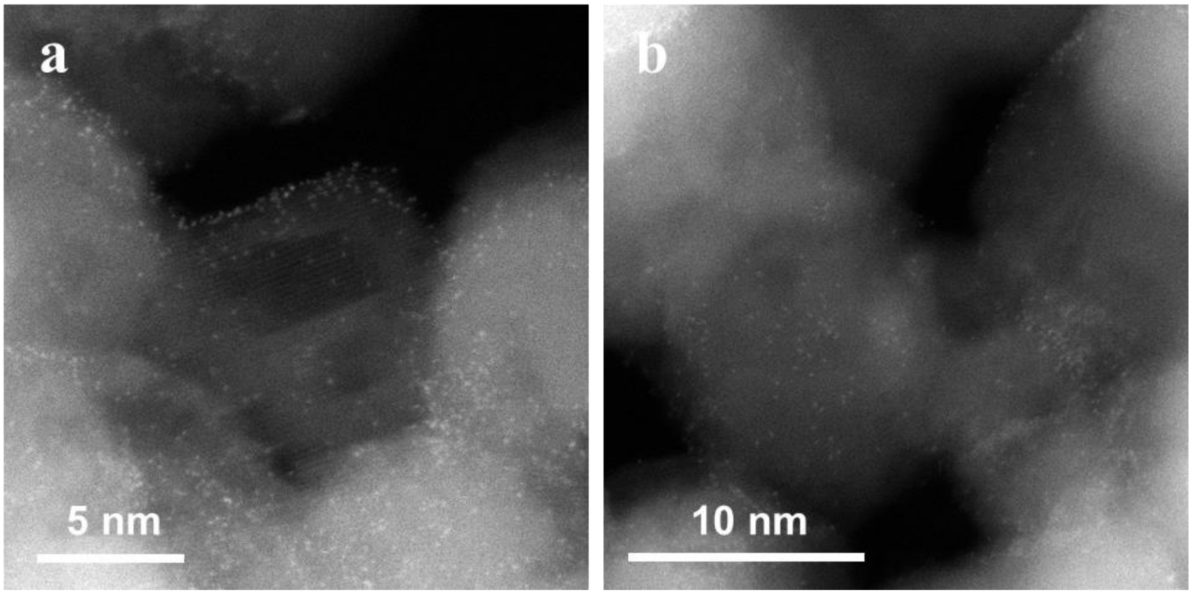

Figure S41. HAADF-STEM images of spent Ce-MgO-D(1.6).

References

1 Lee, S. S. *et al.* High Temperature Decomposition of Cerium Precursors To Form Ceria Nanocrystal Libraries for Biological Applications. *Chem. Mater.* **24**, 424-432, doi:10.1021/cm200863q (2012).

2 Lee, S. S. *et al.* Antioxidant Properties of Cerium Oxide Nanocrystals as a Function of Nanocrystal Diameter and Surface Coating. *ACS Nano* **7**, 9693-9703, doi:10.1021/nn4026806 (2013).

3 Wang, Y. *et al.* Direct Conversion of CO_2 to Ethanol Boosted by Intimacy-Sensitive Multifunctional Catalysts. *ACS Catal.* **11**, 11742-11753, doi:10.1021/acscatal.1c01504 (2021).

4 Kresse, G. & Furthmüller, J. Efficient iterative schemes for ab initio total-energy calculations using a plane-wave basis set. *Phys. Rev. B* **54**, 11169 (1996).

5 Kresse, G. & Hafner, J. Ab initio molecular dynamics for open-shell transition metals. *Phys. Rev. B* **48**, 13115 (1993).

6 Perdew, J. P., Burke, K. & Ernzerhof, M. Generalized gradient approximation made simple. *Phys. Rev. Lett.* **77**, 3865 (1996).

7 Blöchl, P. E. Projector augmented-wave method. *Phys. Rev. B* **50**, 17953 (1994).

8 Grimme, S., Antony, J., Ehrlich, S. & Krieg, H. A consistent and accurate ab initio parametrization of density functional dispersion correction (DFT-D) for the 94 elements H-Pu. *J. Chem. Phys.* **132** (2010).

9 Li, M.-R., Song, Y.-Y. & Wang, G.-C. The Mechanism of Steam-Ethanol Reforming on Co_{13}/CeO_{2-x}: A DFT Study. *ACS Catal.* **9**, 2355-2367, doi:10.1021/acscatal.8b03765 (2019).

10 Henkelman, G., Uberuaga, B. P. & Jónsson, H. A climbing image nudged elastic band method for finding saddle points and minimum energy paths. *J. Chem. Phys.* **113**, 9901-9904, doi:10.1063/1.1329672 (2000).

11 Henkelman, G. & Jónsson, H. Improved tangent estimate in the nudged elastic band method for finding minimum energy paths and saddle points. *J. Chem. Phys.* **113**, 9978-9985 (2000).

12 Henkelman, G. & Jónsson, H. A dimer method for finding saddle points on high dimensional potential surfaces using only first derivatives. *J. Chem. Phys.* **111**, 7010-7022 (1999).

13 Olsen, R., Kroes, G., Henkelman, G., Arnaldsson, A. & Jónsson, H. Comparison of methods for finding saddle points without knowledge of the final states. *J. Chem. Phys.* **121**, 9776-9792 (2004).

14 Xu, L. & Henkelman, G. Calculations of Ca adsorption on a MgO (100) surface: Determination of the binding sites and growth mode. *Phys. Rev. B* **77**, 205404 (2008).

15 Chizallet, C., Costentin, G., Che, M., Delbecq, F. & Sautet, P. Revisiting acido-basicity of the MgO surface by periodic density functional theory calculations: role of surface topology and ion coordination on water dissociation. *J. Phys. Chem. B* **110**, 15878-15886 (2006).

16 Zhu, J. *et al.* Calcium adsorption on MgO (100): Energetics, structure, and role of defects. *J. Am. Chem. Soc.* **130**, 2314-2322 (2008).

17 Zhang, L. *et al.* Highly selective synthesis of light aromatics from CO_2 by chromium-doped ZrO_2 aerogels in tandem with HZSM-5@SiO_2 catalyst. *Appl. Catal. B* **328**, 122535, doi:https://doi.org/10.1016/j.apcatb.2023.122535 (2023).

18 Li, S. *et al.* Tuning the CO_2 Hydrogenation Selectivity of Rhodium Single-Atom Catalysts on Zirconium Dioxide with Alkali Ions. *Angew. Chem. Int. Ed.* **62**, e202218167, doi:https://doi.org/10.1002/anie.202218167 (2023).

19 Zhu, X. *et al.* Selective reduction of carbon dioxide to carbon monoxide over Au/CeO_2 catalyst and identification of reaction intermediate. *Chinese J. Catal.* **37**, 2053-2058, doi:https://doi.org/10.1016/S1872-2067(16)62538-X (2016).

20 Yang, X. *et al.* Promotion effects of potassium on the activity and selectivity of Pt/zeolite catalysts for reverse water gas shift reaction. *Appl. Catal. B* **216**, 95-105, doi:https://doi.org/10.1016/j.apcatb.2017.05.067 (2017).

21 Chen, X. *et al.* Catalytic performance of the Pt/TiO_2 catalysts in reverse water gas shift reaction: Controlled product selectivity and a mechanism study. *Catal. Today* **281**, 312-318,

doi:https://doi.org/10.1016/j.cattod.2016.03.020 (2017).

22 Kim, S. S., Lee, H. H. & Hong, S. C. A study on the effect of support's reducibility on the reverse water-gas shift reaction over Pt catalysts. *Appl. Catal. A-Gen* **423-424**, 100-107, doi:https://doi.org/10.1016/j.apcata.2012.02.021 (2012).

23 Zhao, Z. *et al.* Atomically dispersed Pt/CeO_2 catalyst with superior CO selectivity in reverse water gas shift reaction. *Appl. Catal. B* **291**, 120101, doi:https://doi.org/10.1016/j.apcatb.2021.120101 (2021).

24 Li, W. *et al.* Platinum and Frustrated Lewis Pairs on Ceria as Dual-Active Sites for Efficient Reverse Water-Gas Shift Reaction at Low Temperatures. *Angew. Chem. Int. Ed.* **62**, e202305661, doi:https://doi.org/10.1002/anie.202305661 (2023).

25 Liang, B. *et al.* Promoting role of potassium in the reverse water gas shift reaction on Pt/mullite catalyst. *Catal. Today* **281**, 319-326, doi:https://doi.org/10.1016/j.cattod.2016.02.051 (2017).

26 Wang, L. *et al.* Direct environmental TEM observation of silicon diffusion-induced strong metal-silica interaction for boosting CO_2 hydrogenation. *Nano Res.* **16**, 2209-2217 (2023).

27 Kwak, J. H., Kovarik, L. & Szanyi, J. Heterogeneous Catalysis on Atomically Dispersed Supported Metals: CO_2 Reduction on Multifunctional Pd Catalysts. *ACS Catal.* **3**, 2094-2100, doi:10.1021/cs4001392 (2013).

28 Ye, J., Ge, Q. & Liu, C.-j. Effect of PdIn bimetallic particle formation on CO_2 reduction over the Pd–In/SiO_2 catalyst. *Chem. Eng. Sci.* **135**, 193-201, doi:https://doi.org/10.1016/j.ces.2015.04.034 (2015).

29 Yamano, R., Ogo, S., Nakano, N., Higo, T. & Sekine, Y. Non-conventional low-temperature reverse water–gas shift reaction over highly dispersed Ru catalysts in an electric field. *EES Catalysis* **1**, 125-133, doi:10.1039/D2EY00004K (2023).

30 Wang, L., Liu, H., Liu, Y., Chen, Y. & Yang, S. Effect of precipitants on Ni-CeO_2 catalysts prepared by a co-precipitation method for the reverse water-gas shift reaction. *J. Rare Earths* **31**, 969-974, doi:https://doi.org/10.1016/S1002-0721(13)60014-9 (2013).

31 Kharaji, A. G., Shariati, A. & Ostadi, M. Development of Ni–Mo/Al_2O_3 catalyst for reverse water gas shift (RWGS) reaction. *J. Nanosci. Nanotechnol.* **14**, 6841-6847 (2014).

32 Chen, C.-S., Cheng, W.-H. & Lin, S.-S. Study of iron-promoted Cu/SiO_2 catalyst on high temperature reverse water gas shift reaction. *Appl. Catal. A-Gen* **257**, 97-106, doi:https://doi.org/10.1016/S0926-860X(03)00637-9 (2004).

33 Lu, B. & Kawamoto, K. Preparation of mesoporous CeO_2 and monodispersed NiO particles in CeO_2, and enhanced selectivity of NiO/CeO_2 for reverse water gas shift reaction. *Mater. Res. Bull.* **53**, 70-78, doi:https://doi.org/10.1016/j.materresbull.2014.01.043 (2014).

34 Li, Y. *et al.* Single-atom Co-N-C catalysts for high-efficiency reverse water-gas shift reaction. *Appl. Catal. B* **324**, 122298, doi:https://doi.org/10.1016/j.apcatb.2022.122298 (2023).